Collisional and alteration history of the CM parent body

Lionel Vacher, Yves Marrocchi, Johan Villeneuve, Maximilien Verdier-Paoletti, Matthieu Gounelle

Collisional and alteration history of the CM parent body

Lionel G. Vacher[a*], Yves Marrocchi[a], Johan Villeneuve[a], Maximilien J. Verdier-Paoletti[b] and Matthieu Gounelle[c,d]

[a]CRPG, CNRS, Université de Lorraine, UMR 7358, Vandoeuvre-les-Nancy, F-54501, France

[b]Department of Terrestrial Magnetism, Carnegie Institution of Washington, 5241 Broad Branch Road NW, Washington, DC 20015, USA

[c]IMPMC, MNHN, Sorbonne Universités, UMR CNRS 7590, 57 rue Cuvier, 75005 Paris, France

[d]Institut Universitaire de France, Maison des Universités, 103 boulevard Saint-Michel, 75005 Paris, France

[*]Corresponding author: lvacher@crpg.cnrs-nancy.fr

Keywords:

Clasts, calcite, aragonite, oxygen and carbon isotopes, impacts, X-ray tomography

ABSTRACT

Boriskino is a little studied CM2 chondrite composed of millimeter-sized clasts of different lithologies and degrees of alteration. Boriskino thus offers a good opportunity to better understand the preaccretionary alteration history and collisional evolution that took place on the CM parent body. The least altered lithology displays ^{16}O-poor Type 1a calcite and aragonite grains ($\delta^{18}O \approx 30\text{-}37‰$, $\delta^{17}O \approx 15\text{-}18‰$ and $\Delta^{17}O \approx -2$ to 0‰, SMOW) that precipitated early, before the establishment of the petrofabric, from a fluid whose isotopic composition was established by isotopic exchange between a ^{16}O-poor water and ^{16}O-rich anhydrous silicates. In contrast, the more altered lithologies exhibit ^{16}O-rich Type 2a and veins of calcite ($\delta^{18}O \approx 17\text{-}23‰$, $\delta^{17}O \approx 6\text{-}9‰$ and $\Delta^{17}O \approx -4$ to -1‰, SMOW) that precipitated after establishment of the deformation, from transported ^{16}O-rich fluid in preexisting fractures. From our petrographic and X-ray tomographic results, we propose that the more altered lithologies of Boriskino were subjected to high intensity impact(s) (10-30 GPa) that produced a petrofabric, fractures and chondrule flattening. Taking all our results together, we propose a scenario for the deformation and alteration history of Boriskino, in which the petrographic and isotopic differences between the lithologies are explained by their separate locations into a single CM parent body. Based on the $\delta^{13}C$-$\delta^{18}O$ values of the Boriskino Type 2a calcite ($\delta^{13}C \approx 30\text{-}71‰$, PDB), we propose an alternative $\delta^{13}C$-$\delta^{18}O$ model where the precipitation of Type 2a calcite can occurred in an open system environment with the escape of ^{13}C-depleted CH_4 produced from the reduction of C-bearing species by H_2 released during serpentinization or kamacite corrosion. Assuming a mean precipitation temperature of 110°C, the observed $\delta^{13}C$ variability in T2a calcite can be reproduced by the escape of ≈ 15-50% of dissolved carbon into CH_4 by Rayleigh distillation.

1. INTRODUCTION

The CM carbonaceous chondrites are samples of dark primitive C-type asteroids (Clark et al., 2010; Cloutis et al., 2011) accreted closed to the snowline (Morbidelli et al., 2016) and that contain a high proportion of water (i.e. water/rock ratio = 0.4; Marrocchi et al., 2018), mainly in hydroxyl form in the matrix (Rubin et al., 2007). Their mineralogy and petrography suggest they have undergone brecciation and low temperature hydrothermal alteration, which could have been induced by low velocity impacts and/or by heat released by the decay of the ^{26}Al, respectively (Dufresne and Anders, 1962; Metzler et al., 1992; Zolensky et al., 1997; Nakamura, 2005; Rubin et al., 2007; Nakato et al., 2008). CM chondrites experienced different degrees of aqueous alteration, from moderate (CM2) to high (CM1), as reflected by their varying proportion of secondary phases, including Fe-, Mg- and S-rich phyllosilicates (e.g., sulfide-hydroxide/cronstedtite association, hereafter referred as TCI), Fe-Ni sulfides, and carbonates (McSween, 1979; Bunch and Chang, 1980; Tomeoka and Buseck, 1985; Zolensky et al., 1997; Brearley, 2006; Rubin et al., 2007; Howard et al., 2009, 2015; Hewins et al., 2014; Lee et al., 2014; Pignatelli et al., 2016, 2017; Rubin and Ma, 2017).

Carbonates are ubiquitous in CMs and represent a minor proportion of secondary mineral assemblages (i.e., up to 2-3 vol.%; Marrocchi et al., 2014; Lee et al., 2014). Their mineralogy provides information about the chemical evolution of the fluid during aqueous alteration. For example, Ca-carbonates occur as aragonite and calcite in most CM2 chondrites, whereas dolomites are only found in the more altered CM chondrites (Johnson and Prinz, 1993; Riciputi et al., 1994; Browning and Bourcier, 1998; Benedix et al., 2003; De Leuw et al., 2010; Lee et al., 2012; Lee et al., 2014; Tyra et al., 2016; Vacher et al., 2017). Furthermore, their oxygen isotopic compositions (i.e., $\delta^{17,18}$O) can be used to decipher their precipitation temperature and the origin and evolution of the fluid. Based on the O-isotopic

compositions of Ca-carbonates, it has been proposed (i) that they precipitated at varying temperatures, in the range 0-300°C (Clayton and Mayeda, 1984; Benedix et al., 2003; Guo and Eiler, 2007; Alexander et al., 2015; Verdier-Paoletti et al., 2017a), (ii) that aqueous alteration processes occurred essentially in a closed system with a static fluid interacting with anhydrous silicates (DuFresne and Anders, 1962; Clayton and Mayeda, 1999; Benedix et al., 2003) and (iii) that the least altered CMs (i.e., Paris and Maribo) accreted a significant proportion of ^{17,18}O-rich water inherited from the outer Solar System (Horstmann et al., 2014; Vacher et al., 2016). Carbon isotopic composition of carbonates (δ^{13}C) also reflects aqueous alteration and can constrain the origin of dissolved carbon into the fluid. From bulk and *in situ* C-isotopic compositions of CM carbonates, it has been postulated that carbonates precipitated from C-bearing inorganic molecules (i.e., CO or CO_2; Alexander et al., 2015) or soluble organic matter (SOM) (Vacher et al., 2017). C-isotopes can also be affected by different fractionation mechanisms, such as escape of C-bearing gas (e.g., CH_4, Guo and Eiler, 2007) during, for example, venting event (Telus et al., 2017).

Carbonate precipitation in response to stress events, such as impacts or accretional/gravitational compaction (Cain et al., 1986; Fujimara et al., 1983) has previously been reported based on the presence of different petrographic features: e-twinned calcite, calcite veins and replacement of chondrules by calcite grains (Bunch and Chang, 1980; Benedix et al., 2003; Lee and Ellen, 2008; Lindgren et al., 2011; Tyra et al., 2012; Lee et al., 2014). Calcite veins show ^{16}O-rich isotopic compositions that suggest late precipitation from evolved solutions (Lindgren et al., 2017). This assumption is consistent with a late carbonate precipitation event, during which the evolved fluid would have been mobilized from different region of the parent body or by dehydration of existing phyllosilicates (Rubin, 2012; Lee et al., 2013). In addition, it has been proposed that impacts could create open fracture networks and microcracks in CM chondrites that would facilitate the circulation of fluids (DeCarli et

al., 2001; Rubin, 2012). Impact-induced formation of fractures and/or cracks has been reported in shock experiments involving carbonaceous chondrites (Nakamura et al., 1995; Tomeoka et al., 1999; Nakamura, 2000). These experiments also highlighted the formation of foliation petrofabrics of the chondritic particles (i.e., chondrules, calcium-aluminum-rich refractory inclusions, clumps of tochilinite-cronstedtite intergrowths, olivine grains and flattened aggregates) and the flattening of chondrules with the increase in impact intensity (Nakamura et al., 1995; Tomeoka et al., 1999; Nakamura, 2000). Preferential orientations have been observed in CM and CV chondrites with different degrees of foliation intensity (Rubin, 2012; Lindgren et al., 2015; Hanna et al., 2015). However, impact events are not the only processes able to create preferential orientation of particles; lithostatic compaction may also produce flattened chondrules and CAIs and crystallographic orientation of phyllosilicates and carbonates (Fujimura et al., 1983; Cain et al., 1986; Zolensky et al., 1997; Lee and Ellen, 2008; Lindgren et al., 2015). This latter process was likely involved in the establishment of the CM and CV petrofabrics as attested by (i) the occurrence of preferential orientation in poorly altered CM chondrites without fractures and carbonate veins (Lindgren et al., 2015; Hanna et al., 2015) and (ii) the lack of evidence for strong shock characteristics in some meteorites (Scott et al., 1992). In addition, CM chondrites were probably highly porous prior to their deformation (i.e., 30-50%, Hanna et al., 2015), allowing the impact energy to be dissipated from the collapse of the pore spaces (Suttle et al., 2017). This inconsistency between a low shock-stage and evidence of compaction in CM chondrites (Lindgren et al., 2015) highlights that the relationship between aqueous alteration and stress deformation remains poorly understood.

Most of the CM chondrites are breccias and exhibit clats with various degrees of aqueous alteration (Rubin and Wasson, 1986; Metzler et al., 1992; Lindgren et al., 2013; Bischoff et al., 2017). These clasts provide important constraints on the post-accretionary

alteration history and collisional activity of the CM chondrites (Lindgren et al., 2013). A recent report of the carbonaceous chondrite Boriskino, a CM2 chondrite that fell in Russia in 1930, describes the presence of centimetric clasts with contains clasts with a variety of lithologies (Verdier-Paoletti et al., 2017b), suggesting that this chondrite may provide a good opportunity to better understand the link between aqueous alteration and the deformation history of the CM chondrites that is not well investigated yet. The present study therefore aims to (i) understand the preaccretional alteration history of CM chondrites by characterizing clasts in CM2 Boriskino that exhibit different degrees of alteration, (ii) retrace the isotopic evolution of the fluid from the O & C-isotopic composition of Ca-carbonates, and (iii) identify the mechanisms that induced preferential orientation and aqueous alteration in CM chondrites. From a survey of two Boriskino polished sections, we adopt a multi-pronged approach composed of petrographic observations, preferential orientation measurements on chondritic particles, mineralogical identifications, and O and C-isotopic measurements on Ca-carbonates. We focus our attention on bulk Boriskino samples by performing X-ray computed tomography to map flattening chondrules and measure their preferential orientation.

2. MATERIALS AND METHODS

2-1 SEM imaging, characterizations and petrofabric analyses

Petrographic observations of two polished sections of the Boriskino CM chondrites (#3788-3 and #3788-4) from the Muséum National d'Histoire Naturelle of Paris (MNHN) were made at the Centre de Recherches Pétrographique et Géochimiques (CRPG) using a scanning electron microscope (SEM) JEOL JSM-6510 equipped with an energy dispersive X-ray detector (Bruker-AXS XFlash, silicon drift detector: SDD). The SEM observations were performed with a beam current of 3 nA at 15 kV. The entire two polished sections were mapped to produce the Back-Scattered Electron (BSE) mosaics. The modal abundance of phases for each lithology was determined from the BSE mosaics using JMicroVision software.

Using the BSE mosaics of the two polished sections, the petrofabric characteristics of each clast were determined following the method of Rubin (2012). In order to compare the median orientation of the petrofabrics within each polished section (i.e., #3788-4), we measured the tilt angle between an arbitrary reference (i.e., the horizontal = 0°) and the primary axis length of each particle (i.e., chondrule, TCI clump and olivine grain). The tilt angles were measured using Adobe Illustrator. We then estimated the standard deviation (*c*) of the petrofabric(s), the high maximum frequency (a) and the mean value of the Gaussian curve (b) for each clast using a Gaussian fit on the data set ($y = a \times e^{(\frac{x-b}{c})^2}$).

157 **2-2 Raman spectroscopy**

158

159 Raman spectra were collected using a LabRAM HR spectrometer (Horiba Johin Yvon)
160 equipped with a 600 $g.mm^{-1}$ grating and an Edge filter. The confocal hole aperture and slit
161 aperture were 500 µm and 100 µm, respectively. The excitation beam was produced by a
162 457.94 nm blue laser at a power of ~20mW, focused on the sample using a ×100 LWD IR
163 objective (Olympus). The number of accumulations and the acquisition time were 2x5s. The
164 signal-to-noise ratio (S/N) was less than 1% of the signal. Calcite and aragonite were
165 identified on the basis of their minor Raman bands; calcite has specific bands at 282 and 713
166 cm^{-1} while aragonite has bands at 207 and 704 cm^{-1} (White, 2009).

167

168 **2-3 Carbon and Oxygen isotopes**

169

170 The two polished sections were initially coated with carbon to measure oxygen
171 isotopes. Oxygen isotopic compositions of Ca-carbonates were measured using a CAMECA
172 ims 1280 HR2 at CRPG (Nancy, France). $^{16}O^-$, $^{17}O^-$, and $^{18}O^-$ ions produced by a Cs^+ primary
173 ion beam (≈15 µm spot size, 5 nA) were collected in multi-collection mode using three
174 Faraday cups. A normal-incidence electron gun was used for charge compensation. In order to
175 remove $^{16}OH^-$ interference on the $^{17}O^-$ peak and achieve maximum flatness on the top of the
176 $^{16}O^-$ and $^{18}O^-$ peaks, the entrance and exit slits of the central Faraday cup (80 and 173 µm,
177 respectively) were adjusted to obtain a Mass Resolving Power (MRP = M/ΔM) of ≈ 7000 for
178 $^{17}O^-$ on the central Faraday cup. $^{16}O^-$ and $^{18}O^-$ were measured on L'2 and H1 (slit 1, MRP ≈
179 2500). Acquisition times were set so as to obtain counting statistics on the order of ± 0.2 ‰
180 (1σ) for $\delta^{18}O$ and $\delta^{17}O$. We analysed three terrestrial standards: (i) quartz from Brazil ($\delta^{18}O$ =
181 9.6 ‰, ^{16}O = 1.8 x 10^9 Cps), (ii) forsterite from San Carlos ($\delta^{18}O$ = 5.5 ‰, ^{16}O = 1.7 x 10^9

Cps), and (iii) calcite from Mexico (55.6 wt% of CaO and 0.03 wt% of MgO, $\delta^{18}O$ = 23.6 ‰ and ^{16}O = 2.3 x 10^9 Cps, with a reproducibility 0.3‰, n = 26) to define the Instrumental Mass Fractionation (IMF) for the three oxygen isotopes and correct for instrumental mass fractionation for calcite. $^{17}O/^{16}O$ and $^{18}O/^{16}O$ isotope ratios were normalized using the Standard Mean Ocean Water (SMOW). IMF for both calcite and aragonite was determined from the same Mexico calcite standard because carbonate identification by Raman spectroscopy was performed after isotopic measurements. It should be noted that the matrix effect between calcite and aragonite is negligible (i.e., ≈ 1‰, Lécuyer et al., 2012) regarding the precision of oxygen measurements by SIMS. In addition, the low Fe, Mg and Mn content in Boriskino's Ca-carbonate (i.e., < 1 wt%, Verdier-Paoletti et al., 2017b) is not expected to produce significant IMF (Rollion-Bard et al., 2007). Because IMF values of standards have been observed to derived linearly over the time, we calculated the IMF value for each sample analysis by interpolated its value during time (i.e., number of measurements). Typical measurement errors (2σ), which took into account the errors in each measurement as well as the external reproducibility of the standard, were estimated to be ≈ 0.7 ‰ for $\delta^{18}O$, ≈ 0.6 ‰ for $\delta^{17}O$, and ≈ 0.8 ‰ for $\Delta^{17}O$ (where $\Delta^{17}O$ represents the deviation from the TFL: $\Delta^{17}O = \delta^{17}O - 0.52 \times \delta^{18}O$).

In order to avoid carbon contamination inherited from previous carbon coatings (i.e., after the SEM and O-isotopes), sample surfaces were polished with liquid cerium oxide and ultrasonically cleaned in ethanol for 5 min (Hanon et al., 1998). The samples were then coated with gold (≈ 50 nm) in preparation for carbon isotope analysis using a CAMECA ims 1280 HR2 ion microprobe at CRPG-CNRS (Nancy, France). A Cs^+ primary Gaussian beam of 5 nA was focused to produce a spot size of ≈ 20 μm. A normal-incidence electron gun was used for charge compensation. The microprobe was specifically tuned to obtain a MRP of ≈ 5000 so that the $^{12}CH^-$ contribution to ^{13}C could be eliminated. The settings of the entrance and

multicollector slits (slit 2, Rollion-Bard et al., 2007) and the field aperture were 70 µm, 240 µm and 3000 µm, respectively. Carbon isotopes were measured in multi-collection mode using two off-axis faraday cups, C and H1, with 10^{11} ohm resistors for ^{12}C and ^{13}C, respectively. Before each measurement, a presputtering step of 120s with a raster of 20 x 20 µm was applied in order to remove any remaining traces of the carbon coating. The acquisition time was 5s long and repeated over 40 cycles and the typical internal error for each measurement was ≈ 0.8‰ (2σ) on $\delta^{13}C$. A terrestrial calcite from New Caledonia's carbonatite (55 wt% of CaO and 0.4 wt% of MgO, $\delta^{13}C$ = -5.39 ‰, ^{12}C = 1.4 x 10^7 Cps, Rollion-Bard et al., 2007, with a reproducibility of 0.2 (n = 15) and 0.6 ‰ (n = 8) for sessions 1 and 2, respectively) was used as a standard to correct for Instrumental Mass Fractionation (IMF) for both calcite and aragonite. As for O-isotopes, C-isotopes could be affected by matrix effect. However, the effect of chemical compositions and the aragonite/calcite IMF (≈ 2‰, Lécuyer et al., 2012) is supposed to be negligible considering: (i) the precision on SIMS C-isotopic measurements (i.e., ≈ 1 ‰) and (ii) the large range of $\delta^{13}C$ shown by Ca-carbonates (i.e., 20-90‰). Isotopes ratios were normalized to Pee Dee Belemnite (PDB). Typical measurement errors (2σ), which took into account the errors in each measurement as well as the external reproducibility of the standard, were estimated to be ≈ 0.8 ‰ for $\delta^{13}C$.

2-4 X-ray computed tomography (XCT)

A bulk sample of Boriskino with a mass of 328 mg was subjected to X-ray computed tomography (XCT) imaging to provide a full 3D dataset of the sample (**Fig. 1a**). The CT imaging was made on the AST-RX platform of the Muséum National d'Histoire Naturelle of Paris (MNHN) using a GE Sensing and Inspection Technologies Phoenix|x-ray v|tome|x L240-180 CT scanner. We used the microfocus RX source at 240 kV/320 W, detector 400 × 400 mm, with a matrix of 2024 pixels (pixel size: 200 × 200 microns). The settings

parameters were as follows: voltage = 80 kV; current = 230 µA; exposure: 500 ms; and isotropic voxel size = 8 µm. Data were reconstructed using datos|x reconstruction software (Phoenix|x-ray, release 2.0), then exported into a 16-bit TIFF image stack of 1740 virtual slices in transverse view.

In the full 3D data set of the sample, the grey level of each slice corresponds to the X-ray attenuation, which is related to density and the atomic number of the material. The darkest pixels represent the least attenuating material or the lowest density (e.g., matrix and chondrules) while the brightest pixels represent the most attenuating material or the highest density (e.g., metal and sulphide grains). Thus, based on the grey level of each image, we observed 61 elliptic dark-toned objects that we interpret as type I chondrules (**Fig. 1b**). We painted all voxels into these chondrules on each step of 5 slices for the biggest objects and on each slice for the smallest object with the Avizo^{TM} software. Each chondrule was then modeled in 3D volume by interpolation of the painted voxels. Next, an ellipsoid was fitted to each chondrule by merit function using Blob3D software package (Ketcham, 2005a, Ketcham, 2005b). The orientation, axial length, aspect ratio and location of each ellipsoid were measured (**Table 2**). Plunges, trends and eigenvectors (v_1, v_2 and v_3) of the raw data were calculated and plotted on a stereogram with Stereonet software from the direction cosines given by the Blob3D results. The eigenvalues (λ_1, λ_2 and λ_3) were also determined in order to estimate whether the orientation of the ellipsoids were non-random and defined a petrofabric, according to the method of (Woodcock and Naylor, 1983). In this method, two parameters must be determined: (i) the shape parameter (K), which ranges from K = 0 (girdle distribution) to K >1 (cluster distribution); and (ii) the strength parameter (C), which ranges from C ≈ 0 (weak petrofabric) to C > 4 (strong petrofabric).

3. RESULTS

3.1 Petrography of Boriskino

The two polished sections of Boriskino are composed of millimeter-sized clasts in direct contact with each other, which can be distinguished by their petrography (**Fig. 2**). Among these clasts, we defined three lithologies (labeled 1 to 3) characterized by varying contents of (i) phyllosilicate, (ii) metallic iron, (iii) sulfide, and (iv) different petrographic types of Ca-carbonates (**Fig. 3, Table 1)**.

Lithology 1 is present in both sections of Boriskino and represents 88% and 24% of the sample's surface of section #3 and #4, respectively (**Fig. 2a**). This lithology is characterized by a moderate proportion of matrix and chondrules (≈ 60.15 vol.% and ≈ 30 vol.%, respectively), a high proportion of Fe-Ni sulphide grains (≈ 8.6 vol.%) and a low abundance of Ca-carbonates (≈ 1.2 vol.%) and metallic Fe-Ni (≈ 0.05 vol.%) (**Table 1**; **Fig. 3a**). Lithology 2 is only present in section #4 and corresponds to 26% of the sample's surface, where it is found in two separated clasts. This lithology shows comparable proportions of matrix, chondrules and Ca-carbonate relative to lithology 1 (≈ 62.3 vol.%, ≈ 34.7 vol.% and ≈ 1.4 vol.%, respectively) but a lower proportion of Fe-Ni sulphide (1.6 vol.%) and a lack of Fe-Ni metal (**Table 1**; **Fig. 3b**). Lithology 3 is present in section #4 and represents 22% of the sample's surface, and possibly in section #3 although it is difficult to assess properly due to its low surface area (i.e., 5%, **Fig. 2**). This lithology differs from the others in that it is characterized by a high abundance of matrix and Ca-carbonate (≈ 68.5 vol.% and ≈ 2.4 vol.%, respectively). It has a similar proportion of chondrules to lithology 1 (≈ 23.9 vol.%), a moderate proportion of Fe-Ni sulphide (5.2 vol.%) and a high proportion of Fe-Ni metal (≈ 0.5 vol.%) (**Table 1**; **Fig. 3c**).

3.2 Ca-carbonate grains

Twenty Ca-carbonate grains were observed in the three different lithologies of Boriskino (**Fig. 2**). They mainly occur as calcite in all three lithologies (n = 17, **Table 3**), but a few grains of aragonite were also identified in lithology 3 (n = 4, **Table 3**) (**Fig. 2 & 4**). Based on the mineralogical classification of CM carbonates (Tyra et al., 2007; Tyra et al., 2012; Lee et al., 2014; Vacher et al., 2017), they can be classified into two types: (i) Type 1a grains, which are surrounded by a serpentine/tochilinite rim, and (ii) Type 2a grains, which have replaced primary minerals with inclusions of Fe-Ni sulphide inclusions.

3.2.1 Type 1a Ca-carbonates *(represented in figures as green circles for calcite and diamonds for aragonite)*

Type 1a Ca-carbonates (hereafter T1a) are scattered throughout the matrix of lithology 3 (**Fig. 2a & 2b**). They mostly occur in the form of subhedral or anhedral single or polycrystalline grains with typical sizes in the range from a few tens to hundreds of micrometers (**Fig. 4b**). They are systematically partially or totally surrounded by a serpentine/tochilinite rim with an average thickness of a few micrometers (**Fig. 4a & 4b**). These rims show irregular boundaries at the contacts with the host-grains. The proportions of T1a calcite and aragonite grains are similar, with a fraction of ≈ 66% of calcite (n = 5) and ≈ 44% of aragonite (n = 4). T1a Ca-carbonates have $\delta^{18}O$ values ranging from 29.8 to 36.8‰ (mean of 33.9‰, σ = 2.4‰), $\delta^{17}O$ values from 15.2 to 18.3‰ (mean of 16.7‰, σ = 1‰) and variable $\Delta^{17}O$ values, ranging from -1.8 to -0.4‰ (mean of -1‰, σ = 0.4‰) (**Fig. 5**, **Table 3**). Significant variation in C isotopes is also observed, with $\delta^{13}C$ values between 18.3 and 91.8‰ (mean of 55.8‰, σ = 25.7‰).

3.2.2 Type 2a calcites *(red circles in figures)*

The Type 2a calcites (hereafter T2a) were all found in lithologies 1 and 2, with the exception of grain CC16, which was in lithology 3 (**Fig. 2, Table 3**). They occur as polycrystalline grains of hundreds of micrometers in size containing Fe-Ni sulphide inclusions of a few tens of micrometers in size (**Fig. 4c**). According to their location and morphology, T2a calcites can be divided into two groups: (i) polycrystalline aggregates located in the matrix, exhibiting phyllosilicate and a high proportion of Fe-Ni sulphide (**Fig. 4c**); and (ii) polycrystalline grains that occur in association with phyllosilicates, olivine grains and Fe-Ni sulphide inclusions (**Fig. 7a & 7b**) inside flattened chondrules surrounded by a fine-grained rim (hereafter FGR) (**Fig. 7a & 7b**). T2a calcites show $\delta^{18}O$ values between 17.2 and 22.5‰ (mean of 19‰, σ = 1.4‰), $\delta^{17}O$ values between 6.2 and 8.8‰ (mean of 7.4‰, σ = 0.8‰) and heterogeneous $\Delta^{17}O$ values, ranging from -3.5 to -0.6‰ (mean of -2.5‰, σ = 0.8‰) (**Fig. 5**, **Table 3**). T2a calcites have variable C-isotopic compositions with $\delta^{13}C$ values ranging from 30 to 70.7‰ (mean of 50.1‰, σ = 12.4‰) (**Fig. 6**, **Table 3**).

3.2.3 Veins of calcite *(blue triangles in figures)*

Calcite veins were only identified in lithology 1 (in the #3, **Fig. 2a**) where they occur as polycrystalline grains of hundreds of micrometers in length and tens of micrometers in width (**Fig. 4d**). These veins are in direct contact with the matrix, are free of phyllosilicate, and can contain micrometer-sized Fe-Ni sulphide inclusions. Due to their irregular form and their low thickness, only one successful O-isotopic measurement was carried out, revealing a $\delta^{18}O$ value of 16.9‰ (2σ = 0.6‰), a $\delta^{17}O$ value of 6.7‰ (2σ = 0.5‰) and a $\Delta^{17}O$ value of -2‰

(2σ = 0.7‰). Unfortunately, no C-isotopic composition was successfully measured due to the narrow width of the veins.

3.3 Petrofabric analyses and aspect ratio of type I chondrules

3.3.1 Polished sections

Lithology 1 in section #3 contains several sets of ~200-300 µm fractures and ~100-200 µm veins of calcite orientated in planes near the petrofabric plane (i.e., within 30° of the median azimuth), but also randomly oriented (**Fig. 8a**). Lithologies 1 and 3 in section #3 define a strong petrofabric with 46% and 41%, respectively, of the particle long-axes within 10° of the median azimuth (**Fig. 8a & 8d**). In contrast, lithologies 1 and 2 in section #4 express a weak petrofabric with 26% and 21%, respectively, of the particle long-axes within 10° of the median azimuth (**Fig. 8b & 8c**).

3.3.2 Bulk Boriskino

The orientation of the primary (R1) and tertiary (R3) axis lengths of 61 elliptic type I chondrules were plotted on stereonets in order to determine their degree of preferred alignment (**Fig. 9a & 9b**). According to the method of Woodcock and Naylor (1983), the primary ellipsoid axis orientations of type I chondrules have a girdle distribution, with a shape parameter (K) of 0.6 and a moderately weak foliation fabric strength, with a strength parameter (C) of 1.3 (**Fig. 9a**). The R3 ellipsoid axis orientations of type I chondrules have a cluster distribution, with a shape parameter (K) of 1.9 and a moderately weak foliation fabric strength, with a strength parameter (C) of 1.3 (**Fig. 9b**). Both sample distributions are non-random at the 99% confidence level (S_1/S_3 = 3.77 and S_1/S_3 = 3.61 for R1 and R3, respectively; Woodcock and Naylor, 1983). The diameters and volumes of best-fit chondrule

ellipsoids are variable and range from ~82 to 531 μm (primary axis length) and from 2 to 213 μm^2, respectively (**Table 2**). Their aspect ratios are also heterogeneous, ranging from 1.11 to 3.34 (mean value of 1.87, σ = 0.46, **Table 2**).

4. DISCUSSION

4.1 Oxygen isotopes and sequence of Ca-carbonate precipitation

Boriskino contains two petrographic types of Ca-carbonate depending on the lithology considered: T1a Ca-carbonates (calcite and aragonite) and T2a calcites. T1a Ca-carbonates are ^{16}O-poor (mean $\delta^{18}O$ and $\delta^{17}O$ values of 33.9‰ and 16.7‰, respectively) with a mean and occur as small subhedral grains dispersed throughout the matrix of lithology 3 (**Fig. 5, Table 2**). In contrast, the T2a grains and calcite veins in lithologies 1 and 2 exhibit ^{16}O-rich compositions compared to T1a grains (mean $\delta^{18}O$ and $\delta^{17}O$ values of 19‰ and 7.4‰ respectively, **Fig. 5, Table 2**). Some of the T2a calcites were observed in association with olivine grains and phyllosilicates located within chondrules that are surrounded by FGRs (**Fig. 7a & 7b**). Based on these petrographic and isotopic features, it thus appears that Boriskino's Ca-carbonates define two distinct populations: a first population, made up of T1a calcite and aragonite, with mean $\delta^{18}O$ and $\Delta^{17}O$ values of 33.9‰ (σ = 2.4‰) and -1‰ (σ = 0.4‰) respectively; and a second population, composed of T2a calcite and calcite veins, with $\delta^{18}O$ and $\Delta^{17}O$ values of 18.9‰ (σ = 1.5‰) and -2.5‰ (σ = 0.8‰) respectively (**Fig. 5b**). Taken together, the O-isotopic compositions of Boriskino's Ca-carbonates define a trend with $\delta^{17}O = 0.62 (\pm 0.05) \times \delta^{18}O - 4.3 (\pm 1.3)$ (2σ, R^2 = 0.97; MSWD = 11.6; **Fig. 5a**) that does not fall on the mass-dependent fractionation line (TFL; **Fig. 5a**). This trend is closed, within errors, from those reported in previous studies in different CM chondrites with:

(i) $\delta^{17}O = 0.62 (\pm 0.09) \times \delta^{18}O - 4.1 (\pm 2.8)$ (2σ, R^2 = 0.95, MSWD = 0.26, Tyra et al., 2012)

(ii) $\delta^{17}O = 0.62\ (\pm\ 0.04)\ x\ \delta^{18}O - 4.08\ (\pm\ 1.1)$ (2σ, $R^2 = 0.99$, MSWD = 1.7, Benedix et al., 2003)

(iii) $\delta^{17}O = 0.66\ (\pm\ 0.05) \times \delta^{18}O - 4.7\ (\pm 1.5)$ (2σ, $R^2 = 0.87$, MSWD = 3.3, Verdier-Paoletti et al., 2017a)

(iv) $\delta^{17}O = 0.65\ (\pm\ 0.03) \times \delta^{18}O - 5.4\ (\pm 1.2)$ (2σ, Horstmann et al., 2014).

(v) $\delta^{17}O = 0.70\ (\pm\ 0.03) \times \delta^{18}O - 5.65\ (\pm 1.25)$ (2σ, Lindgren et al., 2017)

The trend with a slope of 0.62 ± 0.05 defined by the Boriskino carbonates (and other CMs) cannot result from precipitation of the carbonates from a common fluid (i.e., with identical $\Delta^{17}O$ values) along a temperature gradient, as this would have produced a slope of 0.52 (**Fig. 10**). Instead, it implies that the main process controlling the O-isotopic compositions of Ca-carbonates relies on variable degrees of isotopic exchanges between a ^{16}O-poor fluid (i.e., a CM primordial water with $\delta^{18}O = 55 \pm 13‰$ and $\delta^{17}O = 35 \pm 9‰$; Fujiya, 2018) and ^{16}O-rich anhydrous silicates (Clayton and Mayeda, 1999). In addition, the trend defined by the Boriskino Ca-Carbonates is, within error, parallel to the CM Water line (i.e., 0.69, Verdier-Paoletti et al., 2017a), and thus supports a mean carbonate precipitation temperature of ≈110°C. However, this isotopic exchange model does not exclude the possibility that small temperature variations could have occurred during the course of alteration, generating a shift in carbonate O-isotopic compositions along a slope of 0.52 for a given degree of isotopic exchange (**Fig. 10**). In such a scenario, the ^{16}O-poor population of Ca-carbonates would have precipitated early in Boriskino's alteration history, while the ^{16}O-rich population would have formed later from more evolved fluids (Fujiya et al., 2016). These two stages of precipitation are also supported by (i) the identification of several aragonite grains in population 1 (**Fig. 4a**) – aragonite is expected to have predated calcite in some other least altered CM chondrites (Sofe, 2013; Lee et al., 2013, 2014; Lindgren et al., 2017; Vacher

et al., 2017), and (ii) the occurrence of chondrule-hosted calcite in population 2 – calcites which are frequently found in other highly altered CM chondrites and are inferred to have formed under extensive episodes of aqueous alteration (Tyra et al., 2012; Lee et al., 2013, 2014; Fujiya et al., 2016). Determining the sequence of precipitation of Boriskino's Ca-carbonates within each population is difficult to assess however. T1a calcites and aragonites are commonly surrounded by Fe-, S- and Si-rich phyllosilicates (**Fig. 4a & 4b**), suggesting that the precipitation of T1a Ca-carbonates predates the formation of phyllosilicates, as already observed in other CM chondrites (Browning and Bourcier, 1998; Lee et al., 2013; Fujiya et al., 2016; Pignatelli et al., 2017, 2018; Vacher et al., 2017). Nevertheless, our isotopic and petrographic results do not allow us to discriminate the formation sequence of T1a calcite and aragonite (**Fig. 5 & 6; Table 3**). In population 2, the T2a calcites were identified in lithologies 1 and 2. These lithologies exhibit high proportions of phyllosilicates compared to lithology 3 (**Table 1**) and show systematic evidence of mafic silicate replacement by serpentine (**Fig. 3a, 3b and 7**). To the contrary, T2a calcites and calcite veins have not been affected by phyllosilicate replacement, as demonstrated by the absence of serpentine rims around these grains (**Fig. 4c, 4d and 7**). Taken together, these results indicate that T2a and veins of calcite precipitated after the formation of phyllosilicates. However, based on our results, no order of precipitation for T2a grains and calcite veins can be inferred.

4.2 A complex deformation history arising from high pressure impact(s)

Our 2D measurements of aligned particles in the three lithologies of Boriskino confirmed that lithologies 1 (section #3) and 3 define a strong petrofabric whereas lithologies 1 (section #4) and 2 exhibit a weak petrofabric (**Fig. 8**). Conceptually, it might appear surprising that, from one section to another, the level of aligned particles can show dramatically different values within a given lithology. However, similar results have already been reported from SEM-BSE images of several faces of a 3D block of Murchison (Lindgren et al., 2015). Significant differences in the level of chondrule alignment were reported, based on the orientation of the sides of the block (20%, 40% and 50% of chondrule long axes within 10° of the median azimuth for +z, -y and +x sides, respectively; Lindgren et al., 2015). Because the Boriskino lithology 1 occurs in two different sections, clasts from lithology 1 could show different spatial orientations, depending on their location on the sample or the orientation of the section cutting and thus, display varying petrographic intensities. Nevertheless, the strongest fabric value measured in lithology 1 (i.e., 46%, **Fig. 8a**) is probably the one with the closest value to the actual maximum. Consequently, we assume that lithology 1 defines a strong petrofarbic despite variations of its particle orientations.

The 3D bulk analyses of type 1 chondrules revealed that Boriskino exhibits a moderately weak foliation fabric (C = 1.3) and a high degree of chondrule flattening (1.87 ± 0.46). This result is consistent with the two XCT studies of Murchison that showed moderately weak petrofabric (R1) and high aspect ratio (C = 1.46, aspect ratio = 1.75 ± 0.39, Lindgren et al., 2015; C = 1.02, aspect ratio = 1.54 ± 0.22, Hanna et al., 2015). A large number of studies have reported chondrule flattening and/or occurrence of petrofabrics in (i) ordinary chondrites (hereafter OCs) (Cain et al., 1986; Stöffler et al., 1991; Scott et al., 1992; Gattacceca et al., 2005; Rubin and Swindle, 2011), (ii) CV chondrites (Nakamura et al., 2000; Watt et al., 2006;

Rubin, 2012) (iii) fined-grained micrometeorites (hereafter FgMMs) (Suttle et al., 2017) and (iv) CM chondrites (Tomeoka et al., 1999; Rubin, 2012; Lindgren et al., 2015; Hanna et al., 2015). Chondrule flattening or petrofabrics are generally interpreted to be the result of impact-induced preferential orientations (Sneyd et al., 1988; Stöffler et al., 1991; Scott et al., 1992; Tomeoka et al., 1999; Nakamura et al., 2000; Gattacceca et al., 2005; Rubin and Swindel, 2011; Rubin, 2012; Lindgren et al., 2015; Hanna et al., 2015; Forman et al., 2016; Suttle et al., 2017) rather than a consequence of lithostatic compaction (Martin and Mills, 1980; Fujimara et al., 1983; Cain et al., 1986; Zolensky et al., 1997; Lee and Ellen, 2008).

Shock metamorphism evidence in OCs was used to propose a comprehensive petrographic classification of their degree of shock (S1 to S6, Stöffler et al. 1991). Based on shock classification, Gattacceca et al. (2005) demonstrated a relationship between the anisotropy of magnetic susceptibility (AMS) and the silicates's shock features in OCs. Collisional evidence was also reported in CV chondrites with (i) the occurrence of S3-S4 petrofabrics (Rubin, 2012) and shock features in olivine and pyroxene grains (Nakamura et al., 1992) and (ii) a strong anticorrelation between their porosity content and their level of shock stage (Gattacceca et al., 2005). More recently, the study of a large number of micrometeorites showed that around 40-80% of FgMMs display petrofabrics, biaxial fabrics and brittle deformation features, indicating that at least some fabrics are impacted at shock pressures > 0.08 GPa. (Suttle et al., 2017). Based on oxygen isotopic compositions as well as textural and geochemistry features, it appears that micrometeorites are related to CM chondrites (Kurat et al., 1994; Brownlee et al., 1997; Genge et al., 1997; Suavet et al., 2010; Gounelle et al., 2005). Although CM chondrites contain shock compaction features similar to FgMMs, (Lindgren et al., 2011; 2015; Rubin, 2012; Hanna et al., 2015), they do not contain high grade shock features (i.e., > S1-S2; Scott et al., 1992). This contradiction might be related to the capability of porous CMs to absorb and dissipate impact energy due to collapse of the pore

space (Suttle et al., 2017). A such process has been demonstrated in Murchison with (i) the observation of squeezed chondrules resulting from a component of noncoaxial shear induced by impact and (ii) the loss of ≈10-31% of chondrule bulk porosity after shock compactions (Hanna et al., 2015). In Boriskino, we also observed squeezed chondrules within lithology 1 (#4, **Fig. 7c**). Other evidence of impact-induced CM petrofabrics has been highlighted in different studies, including the regolith-brecciated nature of CMs (Metzler et al., 1992; Rubin, 2012) and multiple episodes of deformation recorded by a calcite vein in the LON 94101 CM (Lindgren et al., 2011).

Shock recovery-experiments were performed on CM2 and CV3 chondrites and successfully reproduced the flattened shapes of chondrules and their petrofabrics (Nakamura et al., 1995; 2000; Tomeoka et al., 1999). These experiments were carried out at various peak pressure intensities on Murchison (4-49 GPa) and Allende (11-21GPa) and demonstrated a good correspondence between the aspect ratio of CM and CV chondrules and impact pressures (**Fig. 11**). From these experimental correlations, it is possible to quantitatively estimate the intensity of *a single impact* that induced the chondrule aspect ratio in Boriskino. The mean XCT chondrule aspect ratio of 1.87 ± 0.46 (**Table 2**) corresponds to impacts with intensities ranging from 18 to > 30 GPa and 8-31 GPa, taking into account the experiment results obtained on Murchison and Allende, respectively (**Fig. 11**; Tomeoka et al., 1999; Nakamura et al., 2000). They are consistent with those determined in the CMs MET 01072, Murchison and LAP 031166 (Lindgren et al., 2015; Hanna et al., 2015) (**Fig. 11**). Taken together, our results suggest that some of the CMs probably underwent high intensity impacts. Nevertheless, shock pressure estimations should be treated with caution as they represent the effect of only a single impact on the parent body. Because Boriskino represents the final assemblage of several clasts of different lithology and deformation degree, it seems unlikely that each clast experienced the same collisional history. In addition, the pressure estimates

determined from shock-recovery experiments on Murchison suggest a high intensity of shock pressure, with pressures that may have exceeded 30 GPa and which should have induced melting of the matrix and chondrules (Tomeoka et al., 1999). However, no evidence for melting has been observed in Boriskino.

To summarize, there are several lines of evidence for shock features in Boriskino, including (i) a strong 2D petrofabric in different lithologies, (ii) flattened chondrules, (iii) calcite veins and fractures subparallel to the petrofabric, (iv) squeezed chondrules, and (v) millimeter clasts of various petrographies in direct contact with each other. Based on these observations, we suggest that some of the clasts that make up the Boriskino meteorite (i.e., clasts composed of lithologies 1 and 2) were subjected to high intensity impact(s) (i.e., 10-30 GPa) that produced petrofabrics, chondrule flattening, and fractures.

519 **4.3 Relationship between aqueous alteration and impacts**

520

521 Understanding the relative timing between deformation and aqueous alteration in
522 chondrites is crucial, because it can provide constraints on the conditions of parent-body
523 alteration (Brearley, 2006). It is commonly accepted that aqueous alteration of CM chondrites
524 took place on their parent body(-ies) due to heat released by the decay of ^{26}Al (Dufresne and
525 Anders, 1962; Zolensky et al., 1997). Shock compaction has also been advanced as a principal
526 alteration process in CM chondrites (Greenwood et al., 1994; Rubin, 2012; Lindgren et al.,
527 2015; Hanna et al., 2015). Based on a strong correlation between the degree of alteration and
528 the intensity of impact compaction (**Fig. 12**), Rubin (2012) proposed that random collisions
529 may induce the formation of fractures and favor the mobilization of liquid water by
530 dehydration of phyllosilicates or the melting of ice. This is also supported by the occurrence
531 of dolomite veins with similar orientation to their respective petrofabrics in the highly altered
532 CM2 QUE 93005 and CM1 SCO 06043 (Lindgren et al., 2015). Other reported petrographic
533 evidence for impact-induced alteration includes (i) serpentine veins parallel to the foliation
534 fabric in Murchison (Hanna et al., 2015) and (ii) millimeter lenses rich in phyllosilicates, Ni-
535 bearing sulfide and Ca-phosphate grains subparallel to fractures and elongated chondrules in
536 the CM1 MET 01070 (Rubin et al., 2007; Lindgren et al., 2012). The latter suggests the
537 precipitation of secondary minerals from transported fluid in preexisting fractures (Rubin,
538 2012). In Boriskino, lithologies 1 and 2 exhibit petrographic features consistent with a high
539 degree of alteration (i.e., petrologic subtype expected to be 2.1) as demonstrated by the
540 (i) partial alteration of mafic silicates into chondrules (**Fig. 3a & 3b**), (ii) low metallic Fe-Ni
541 content (≤ 0.05 vol.%, **Table 1**) and (iii) occurrence of ^{16}O-rich T2a grains (**Fig. 5a,** Rubin,
542 2012). Lithologies 1 and 2 also define strong and weak petrofabrics (i.e., 26 and 46% for
543 lithology 1, respectively, **Fig. 8a and b**) that probably result from different spatial

orientations (also expected for the lithology 2 due to its weak petrofabric) and/or separate section's positions on the cutting plane. However, considering the strongest fabric measured as the closest value to the actual maximum (i.e., 41%, **Fig. 8a**), the relationship between degree of alteration *vs* strength of the petrofabric for the lithology 1 is consistent with the correlation defined by Rubin (2012) and thus favour models of impact-induced alteration (**Fig. 12**). In addition, the occurrence of large calcite veins subparallel to the petrofabric (**Fig 4a and 8a**) and the replacement of primary elongated chondrules by T2a calcite (**Fig. 7a & b**) also support this type of alteration process. For the lithology 2, the lack of calcite vein and the weak intensity of its fabric are more problematic, but according to petrographic observations (i.e., T2a grains and replacement of elongated chondrules), we assumed similar alteration process than for the lithology 1.

In contrast, lithology 3 presents characteristics consistent with a lower degree of alteration (i.e., presumed to be petrologic subtype 2.5-2.6; Rubin, 2015), due to: (i) unaltered mafic silicates into chondrules (**Fig. 3c**), (ii) a significant abundance of Fe-Ni metal beads (i.e., ~0.5 vol.%, **Table 1**) and (iii) the presence of ^{16}O-poor T1a calcite and aragonite. Furthermore, lithology 3 does not show any petrographic features characteristics of impact-induced fluid circulation within fractures (e.g., vein of carbonate). Instead, this lithology appears to contain undistorted Ca-carbonates wrapped by phyllosilicates (**Fig. 13a**), stretched clumps of phyllosilicates, and elongate sulphide grains parallel to the petrofabric (**Fig. 13b**). These observations suggest that secondary minerals precipitated before the formation of the petrofabric and that aqueous alteration predates the deformation. Furthermore, by reporting the petrofabric intensity (i.e., 41%) as function of the expected CM subtype of the lithology 3 (**Fig. 12**), it is observed that the percentage of particles with long axes within 10° is to high compared to the predicted value from the correlation of Rubin (2012) (i.e., ≈ 15%, **Fig. 12**). The strong petrofabric observed in the lithology 3 probably results on later episodes of

569 deformation that have not affected alteration but only increased the preferential orientation of
570 particles in the lithology 3 (**Fig. 12**).

571 Our results demonstrate that Boriskino is a clastic polymict breccia, composed of various
572 lithologies, in direct contact with each other, that display different degrees of alteration and
573 deformation histories. Based on our petrographic and isotopic results, we propose a
574 deformation and alteration history for Boriskino based on a single CM parent body, where the
575 different clasts of the breccia chondrite come from different regions of the asteroid (**Fig. 14a**)
576 (Scott and Taylor, 1983; Lindgren et al., 2013). At time t_1 in our scenario, aqueous alteration
577 processes were initiated through the melting of ice induced by ^{26}Al decay within the parent
578 body (**Fig. 14a**). Hence, the ^{16}O-poor primitive fluid interacts with the ^{16}O-rich anhydrous
579 components of the parent body to precipitate isolated aragonite and calcite grains in the
580 matrix as observed in lithology 3. Then, as alteration progresses, the chemical composition of
581 the fluid changes, stopping the precipitation of T1 carbonate and initiating phyllosilicate
582 formation. We do not exclude the possibility that these events occurred in lithologies 1 and 2
583 as well, but to date, no evidence for these events has been observed. Next, at time t_2, one or
584 several high intensity impacts induced the formation of fractures and petrofabrics and the
585 stretching of chondrules, principally in lithologies 1 and 2 due to their location close to the
586 impact zone (**Fig. 14b**). Subsequently, at time t_3, the establishment of cracks and fractures
587 favored the circulation of evolved ^{16}O-rich fluids within the parent body (**Fig. 14c**). This late
588 fluid flow would have allowed the formation of phyllosilicate and T2 carbonate in chondrules
589 and the precipitation of veins of calcite in fractures (**Fig. 14c**). Finally, at time t_4, a new
590 episode of low intensity impact(s) generated the release of all Boriskino's clasts from their
591 initial locations, making possible the mixing of the different altered lithologies together to
592 form the clastic polymict breccia Boriskino (**Fig. 14d**).
593

4.4 Carbon and oxygen isotopes

The *in situ* $\delta^{13}C$-$\delta^{18}O$ compositions of Ca-carbonates in Boriskino are consistent with those reported in other CM carbonates (**Fig. 15**; Fujiya et al., 2015, 2016; Tyra et al., 2016; Telus et al., 2017; Vacher et al., 2017). Our results show that Boriskino's Ca-carbonates exhibit two different populations with distinct $\delta^{18}O$ values and significant variations in $\delta^{13}C$ values (i.e., $\delta^{18}O \approx 35‰$, $\delta^{13}C \approx$ 20-90 ‰ and $\delta^{18}O \approx 20‰$, $\delta^{13}C \approx$ 30-70‰ for T1a and T2a, respectively). Furthermore, these Ca-carbonates do not show positive or negative $\delta^{13}C$-$\delta^{18}O$ correlations, whether for all the dataset or within each population (**Fig. 15**). Because the fractionation factor of C isotopes between calcite and HCO_3^- in the fluid is small at 0-300°C (i.e., $1000\ln\alpha_{calcite\text{-}HCO3^-} \approx$ 1-2 ‰; Deines et al., 1974; Luo and Wang, 2009), the $\delta^{13}C$ values of Ca-carbonates are useful for (i) tracking the source of carbon involved in their precipitation (Grady et al., 1988; Alexander et al., 2015; Fujiya et al., 2015; Vacher et al., 2017) and (ii) identifying fractionation mechanisms, such as equilibrium or kinetic isotope fractionation (e.g., production of CH_4 or loss of C-bearing gas from the fluid during serpentinization or degassing events, respectively; Guo and Eiler, 2007; Fujiya et al., 2016; Telus et al., 2017).

The C and O-isotopic compositions of Boriskino's Ca-carbonates can be explained in numerous ways. Their $\delta^{13}C$-$\delta^{18}O$ values can be reproduced by the equilibration of a CO gas ($\delta^{13}C_{CO} = -33‰$) with different mole fraction of CO_2 in a ^{16}O-rich aqueous fluid ($\delta^{18}O = 5‰$) at low temperature (≈ 0-30°C and ≈ 80-120°C for T1a and T2a, respectively; Alexander et al., 2015) (**Fig. 16a**). They can also be the result from different fluids derived from variable O-isotopic equilibration and contributions of different ^{12}C- and ^{13}C-rich water-soluble organic compounds (SOM) which demonstrated similar range of $\delta^{13}C$ values (i.e., -10 to 60‰, **Fig. 16a**, Vacher et al., 2017). However, these two models consider a closed-system alteration without the escape of C-bearing species. As demonstrated by our petrographic results, T2a

calcites occur in lithologies that have probably undergone multiple episodes of shock compactions causing the formation of cracks and fractures. Under such conditions, the closed-system is merely an approximation; highly diffusive gas such as C-bearing molecules (e.g., CO_2 or CH_4) likely escaped rapidly from the shocked regions. Such a process has been put forward to explain the occurrence of two distinct isotopic groups of calcite in CM MET 01070, characterized by (i) high $\delta^{18}O$ and variable $\delta^{13}C$ compositions, and (ii) low $\delta^{18}O$ and high $\delta^{13}C$ values (**Fig. 15;** Telus et al., 2017). The authors interpreted this shift in $\delta^{13}C$ values as the result of a venting event, in agreement with the petrographic evidence of fluid flow in MET 01070 (Rubin et al., 2007). Based on a negative $\delta^{13}C$-$\delta^{18}O$ correlation observed in CM carbonates, it has been also proposed that carbonate precipitation was accompanied by the production of ^{13}C-depleted CH_4 and its escape from the CM parent body (Guo and Eiler, 2007). However, as highlight in terrestrial environment, abiotic methane is not produced directly by serpentinization, but through the reduction of various C-bearing (e.g., CO, CO_2 or HCO_3^-) species by H_2 during Fischer Tropsch type (FTT) or Sabatier processes (Proskurowski, 2010; Etiope and Sherwood Lollar, 2013):

$$HCO_3^- + 4H_2 = CH_4 + H_2O + OH^- \quad \text{(in aqueous phase; Horita and Berndt, 1999)} \qquad (1)$$

In CM chondrites, H_2 is believed to form during the serpentinization of olivine/pyroxene minerals (Pignatelli et al., 2017) and/or the corrosion of kamacite grains (Palmer and Lauretta, 2011). Reaction kinetics of FTT or Sabatier processes are theoretically much efficient at high temperature than at lower temperatures (<100ºC). Nevertheless, CH_4 production could be significant at low temperature due to the action of different catalyses, such as chromite, magnetite or Fe-Ni alloys (Horita and Berndt, 1999; Foustoukos and Seyfried, 2004) which occur in CM chondrites (Brearley, 2006; Hewins et al., 2014).

Because T2a calcites have precipitated after the formation of fractures and petrofabrics in the lithologies 1 and 2, we propose that the variability in the $\delta^{13}C$ values can reflects the

644 release of ^{13}C-depleted CH_4 produced by FFT or Sabatier reactions through cracks induced by
645 high intensity impact(s). We also considered that escape of CH_4 has been limited for T1a
646 carbonates because they probably formed prior serpentine (Lee et al., 2014; Vacher et al.,
647 2017) and thus, they are no include in the model. Furthermore, escape of CO_2 is not taking
648 account in this model, because carbon dioxide is preferentially release in acid environment
649 (e.g., at pH = 4-6 in terrestrial evaporating Dead Sea brines, Stiller et al., 1985) whereas
650 alteration in CM chondrites appears to occur in alkaline environment (Palmer and Lauretta,
651 2011; Zolotov, 2014; Pignatelli et al., 2016; 2017). Assuming an aqueous fluid with dissolved
652 HCO_3^-, CH_4 and CO_2 at isotopic equilibrium in an open system model, the amount of can be
653 calculated using a Rayleigh-type isotopic equation:

654 $$R_{HCO_3^-} = R_{HCO_3^-{}_0} \times f^{(\alpha_{(HCO_3^-/CH_4)}-1)} \qquad (2)$$

655 where $R_{HCO_3^-}$ is the isotopic ratio of the HCO_3^- after a certain amount of Rayleigh distillation,
656 $R_{HCO_3^-{}_0}$ is the initial isotopic ratio of HCO_3^-, f is the fraction of phase HCO_3^- remaining, and
657 $\alpha_{HCO_3^-/CH_4}$ is the equilibrium fractionation factor between HCO_3^- and CH_4. By incorporating
658 the delta notation (i.e., $\delta^{13}C$) instead of the isotopic ratio ($^{13}C/^{12}C$) in Eqn. (1), we obtain the
659 following equation:

660 $$\delta^{13}C_{HCO_3^-} = \left[\left(1000 + \delta^{13}C_{HCO_3^-{}_0}\right) \times f^{(\alpha_{(HCO_3^-/CH_4)}-1)}\right] - 1000 \qquad (3)$$

661 Hence, the estimates of the C-isotopic compositions of the fluid (i.e., the $\delta^{13}C_{HCO_3^-}$ values) for
662 different amounts of HCO_3^- escape are dependent on (i) the initial C-isotopic composition of
663 the fluid (i.e., the $\delta^{13}C_{HCO_3^-{}_0}$ value) and (ii) the equilibrium fractionation factor between
664 HCO_3^- and CH_4, which is a direct function of the temperature. This calculation is also linked
665 to a fundamental assumption, that the oxygen isotopes of the water constitute an infinite
666 reservoir and thus, the O-isotopic composition of the fluid is not affected by the Rayleigh
667 distillation.

Interestingly, the *in situ* $\delta^{13}C$-$\delta^{18}O$ values of CM2 and CM1 Ca-carbonate define two similar trends (except for the $\delta^{13}C$-$\delta^{18}O$ values of MET 01070) with their C-isotopic compositions converging toward a low range of $\delta^{13}C$ values for a high degree of O-isotopic equilibration (i.e., $\delta^{13}C_{calcite} \approx$ 20-30‰) (**Fig. 15**). Furthermore, by including the $\delta^{13}C$-$\delta^{18}O$ values of the type 1 and type 2 calcites from the CM2 Nogoya (Fujiya et al., 2016), these two groups exhibit constant $\delta^{13}C$ values for different O-isotopic compositions (excluding 2 points from the type 2) at $\delta^{13}C_{calcite} \approx$ 30‰ ($\sigma \approx$ 4‰) (**Fig. 16b**). As the lowest $\delta^{13}C$ value of the T2a calcite in Boriskino displays similar C-isotopic composition to the Nogoya calcites and the two CM tendencies (i.e., $\delta^{13}C_{calcite}$ = 30‰ for the CC9 grain), we assume that this value represents the initial $\delta^{13}C_{HCO_{3_0}^-}$ of the fluid. Interestingly, this value is consistent with the range of C-isotopic values of the SOM reported by Sephton and Botta (2005) in Murchison. Thus, by combining the carbon equilibrium fractionation factors of HCO_3^-/CO_2 (5-125°C, Mook et al., 1974) and CO_2/CH_4 (0-700°C, Bottinga, 1969), we can determine the equilibrium fractionation factor of HCO_3^-/CH_4 for a given temperature. Assuming a mean temperature of precipitation for T2a calcites of 110°C, the equilibrium fractionation factor of HCO_3^-/CH_4 is 0.9535 at 110°C ($1000\ln\alpha_{CH4\text{-}HCO3^-}$ = -47.6‰). Hence, the observed $\delta^{13}C$ variabilities in T2a calcite in Boriskino (i.e., $\delta^{13}C_{calcite}$ = 38-65‰, **Table 3**) can be explained by a loss of ≈ 15-50% of dissolved carbon from the fluid into CH_4. We note that this estimate is largely temperature dependent, and different results will be found at other temperatures (Fujiya et al., 2016).

5. CONCLUSIONS

Brecciation is common in CM chondrites and understanding the origin of individual lithologies recorded among clasts in breccia can provide constraints on the preaccretionnary

693 alteration history and collisional activity that took place on their parent body. From a
694 petrographic and isotopic survey of Ca-carbonates in the clastic breccia CM2 Boriskino, we
695 have investigated and traced the relative timings of deformation and aqueous alteration of the
696 CM parent body. The principal results of this paper are:

697 (1) Boriskino is composed of millimeter clasts, in direct contact with each other, that
698 display various lithologies characterized by different degrees of alteration and
699 deformation histories.

700 (2) The least altered lithology (lithology 3) contains Type 1a Ca-carbonates that are
701 surrounded by phyllosilicates. Type 1a Ca-carbonates are ^{16}O-poor and precipitated
702 early in Boriskino's alteration history. This is interpreted as the result of isotopic
703 exchange between a ^{16}O-poor fluid and ^{16}O-rich anhydrous silicates in a closed-system
704 model. Petrographic observations suggest that secondary minerals formed before the
705 establishment of the petrofabric, and thus that alteration predated the deformation.

706 (3) The more altered lithologies (lithologies 1 & 2) are composed of ^{16}O-rich Type 2a Ca-
707 carbonates (calcites) and veins of calcite lying subparallel to the petrofabric. These
708 calcites precipitated after the establishment of the deformation, from transported ^{16}O-
709 rich fluid in preexisting fractures and cracks.

710 (4) Based on strong evidence of shock features in Boriskino, we propose that some of the
711 clasts that make up the Boriskino meteorite were subjected to high pressure impact(s)
712 (i.e., 10-30 GPa) that generated strong petrofabrics, chondrule flattening and fractures.

713 (5) Taking all our results together, we propose a reconstruction of the deformation and
714 alteration history of Boriskino in which the different lithologies are explained by their
715 separate positions into the CM parent body. Assuming multiple shock compaction
716 events, the occurrence of a strong petrofabric, calcite veins and elongated chondrules
717 in the more altered lithologies could be explained by their location close to the impact

zone, promoting a late circulation of fluid flow into fractures.

(6) Based on the C-isotopic composition of Boriskino Ca-carbonates, we propose that the formation of T2a calcite probably can took place in an open system environment with a loss of ^{13}C-depleted CH_4 produced from the reduction of C-bearing species by H_2 released during serpentinization or kamacite corrosion (Guo and Eiler, 2007). Considering a mean precipitation temperature of Ca-carbonates of 110°C, an escape of ≈ 15-50% of dissolved carbon into CH_4 by Rayleigh distillation is able to reproduce the range of C-isotopic compositions observed in T2a calcites.

ACKNOWLEDGMENTS

We are very grateful to Nordine Bouden for his helpful assistance with the carbon and oxygen isotope measurements, to Patricia Wils and the AST-RX UMS 2700 MNHN technical facilities for their technical support with the XCT analyses and to Marie-Camille Caumon for her assistance with the Raman analyses. We also thank the Muséum National d'Histoire Naturelle de Paris (MNHN) for the loan of the Boriskino samples. This work was funded by l'Agence Nationale de la Recherche through grant ANR-14-CE33-0002-01 SAPINS (PI Yves Marrocchi). This is a CRPG contribution#2568 And SAPINS contribution #11.

REFERENCES

Alexander C. M. O., Bowden R., Fogel M. L. and Howard K. T. (2015) Carbonate abundances and isotopic compositions in chondrites. *Meteorit. Planet. Sci.* **50**, 810–833.

Benedix G., Leshin L., Farquhar J., Jackson T. and Thiemens M. (2003) Carbonates in CM2 chondrites: constraints on alteration conditions from oxygen isotopic compositions and petrographic observations. *Geochim. Cosmochim. Acta* **67**, 1577–1588.

Bischoff A., Ebert S., Metzler K. and Lentfort S. (2017) Breccia classification of CM chondrites. In *80th Annual Meeting of the Meteoritical Society*. #6089 (abstr.).

Bottinga Y. (1969) Calculated fractionation factors for carbon and hydrogen isotope exchange in the system calcite-carbon dioxide-graphite-methane-hydrogen-water vapor. *Geochim. Cosmochim. Acta* **33**, 49–64.

Brearley A. J. (2006) The action of water. *Meteor. Early Sol. Syst. II* **943**, 587–624.

Browning L. B. and Bourcier W. L. (1998) On the Origin of Rim Textures Surrounding Carbonate Grains in CM Matrices. In *Lunar and Planetary Science Conference* Lunar and Planetary Inst. Technical Report.

Brownlee D. E., Bates B., and Schram L. (1997) The elemental composition of stony cosmic spherules. *Meteorit. Planet. Sci.*, **32**, 157–175.

Bunch T. E. and Chang S. (1980) Carbonaceous chondrites—II. Carbonaceous chondrite phyllosilicates and light element geochemistry as indicators of parent body processes and surface conditions. *Geochim. Cosmochim. Acta* **44**, 1543–1577.

Cain P. M., McSween H. Y. and Woodward N. B. (1986) Structural deformation of the Leoville chondrite. *Earth Planet. Sci. Lett.* **77**, 165–175.

Clark B. E., Ziffer J., Nesvorny D., Campins H., Rivkin A. S., Hiroi T., Barucci M. A., Fulchignoni M., Binzel R. P., Fornasier S., DeMeo F., Ockert-Bell M. E., Licandro J. and Mothé-Diniz T. (2010) Spectroscopy of B-type asteroids: Subgroups and meteorite analogs. *J. Geophys. Res. Planets* **115**, 1-22.

Clayton R. N. and Mayeda T. K. (1999) Oxygen isotope studies of carbonaceous chondrites. *Geochim. Cosmochim. Acta* **63**, 2089–2104.

Clayton R. N. and Mayeda T. K. (1984) The oxygen isotope record in Murchison and other carbonaceous chondrites. *Earth Planet. Sci. Lett.* **67**, 151–161.

Cloutis E. A., Hiroi T., Gaffey M. J., Alexander C. M. O. and Mann P. (2011) Spectral reflectance properties of carbonaceous chondrites: 1. CI chondrites. *Icarus* **212**, 180–209.

DeCarli P. S., Bowden E. and Seaman L. (2001) Shock-induced compaction and porosity in meteorites. In *64th Annual Meeting of the Meteoritical Society*. #5171 (abstr.).

De Leuw S., Rubin A. E. and Wasson J. T. (2010) Carbonates in CM chondrites: Complex formational histories and comparison to carbonates in CI chondrites: Carbonates in CM chondrites. *Meteorit. Planet. Sci.* **45**, 513–530.

Deines P., Langmuir D. and Harmon R. S. (1974) Stable carbon isotope ratios and the existence of a gas phase in the evolution of carbonate ground waters. *Geochim. Cosmochim. Acta* **38**, 1147–1164.

Dufresne E. R. and Anders E. (1962) On the chemical evolution of the carbonaceous chondrites. *Geochim. Cosmochim. Acta* **26**, 1085–1114.

Etiope G. and Sherwood Lollar B. (2013). Abiotic Methane On Earth. *Reviews of Geophysics*, 51(2012), 276–299.

Forman L. V., Bland P. A., Timms N. E., Collins G. S., Davison T. M., Ciesla F. J., Benedix G. K., Daly L., Trimby P. W., Yang L. and Ringer S. P. (2016) Hidden secrets of deformation: Impact-induced compaction within a CV chondrite. *Earth Planet. Sci. Lett.* **452**, 133–145.

Foustoukos D. I. and Seyfried W. E. (2004) Hydrocarbons in hydrothermal vent fluids: the role of chromium-bearing catalysts. *Science* **304**, 1002–1005.

Fujimura A., Kato M. and Kumazawa M. (1983) Preferred orientation of phyllosilicate [001] in matrix of Murchison meteorite and possible mechanisms of generating the oriented texture in chondrites. *Earth Planet. Sci. Lett.* **66**, 25–32.

Fujiya W. (2018) Oxygen isotopic ratios of primordial water in carbonaceous chondrites. *Earth Planet. Sci. Lett.* **481**, 264–272.

Fujiya W., Sugiura N., Marrocchi Y., Takahata N., Hoppe P., Shirai K., Sano Y. and Hiyagon H. (2015) Comprehensive study of carbon and oxygen isotopic compositions, trace element abundances, and cathodoluminescence intensities of calcite in the Murchison CM chondrite. *Geochim. Cosmochim. Acta* **161**, 101–117.

Fujiya W., Fukuda K., Koike M., Ishida A. and Sano YA. (2016) Oxygen and carbon isotopic ratios of carbonates in the Nogoya CM chondrite. *Lunar Planet. Sci. 47*. Lunar Planet. Inst., Houston. #1712 (abstr.).

Gattacceca J., Rochette P., Denise M., Consolmagno G. and Folco L. (2005) An impact origin for the foliation of chondrites. *Earth Planet. Sci. Lett.* **234**, 351–368.

Genge M. J., Grady M. M. and Hutchison R. (1997) The textures and compositions of fine-grained Antarctic micrometeorites: Implications for comparisons with meteorites. *Geochim. Cosmochim. Acta* **61**, 5149–5162.

Gounelle M., Engrand C., Maurette M., Kurat G., McKeegan K. D. and Brandstätter F. (2005) Small Antarctic micrometeorites: A mineralogical and in situ oxygen isotope study. *Meteorit. Planet. Sci.* **40**, 917-932.

Grady M. M., Wright I. P., Swart P. K. and Pillinger C. T. (1988) The carbon and oxygen isotopic composition of meteoritic carbonates. *Geochim. Cosmochim. Acta* **52**, 2855–2866.

Greenwood R. C., Lee M. R., Hutchison R. and Barber D. J. (1994) Formation and alteration of CAIs in Cold Bokkeveld (CM2). *Geochim. Cosmochim. Acta* **58**, 1913–1935.

Guo W. and Eiler J. M. (2007) Temperatures of aqueous alteration and evidence for methane generation on the parent bodies of the CM chondrites. *Geochim. Cosmochim. Acta* **71**, 5565–5575.

Hanna R. D., Ketcham R. A., Zolensky M. and Behr W. M. (2015) Impact-induced brittle deformation, porosity loss, and aqueous alteration in the Murchison CM chondrite. *Geochim. Cosmochim. Acta* **171**, 256–282.

Hanon P., Robert F. and Chaussidon M. (1998) High carbon concentrations in meteoritic chondrules: A record of metal-silicate differentiation. *Geochim. Cosmochim. Acta* **62**, 903–913.

Hewins R. H., Bourot-Denise M., Zanda B., Leroux H., Barrat J.-A., Humayun M., Göpel C., Greenwood R. C., Franchi I. A., Pont S., Lorand J.-P., Cournède C., Gattacceca J., Rochette P., Kuga M., Marrocchi Y. and Marty B. (2014) The Paris meteorite, the least altered CM chondrite so far. *Geochim. Cosmochim. Acta* **124**, 190–222.

Horita J. and Berndt M. E. (1999) Abiogenic methane formation and isotopic fractionation under hydrothermal conditions. *Science* **285**, 1055–1057.

Horita J., Ueda A., Mizukami K., and Takatori I. (1989) Automatic δD and $\delta^{18}O$ analyses of multi-water samples using H_2-water and CO_2-water equilibration methods with a common equilibration set-up. *Appl. Rad. Isot*. **40**: 801-805.

Horstmann M., Vollmer C., Birth M. I. F., Chaussidon M., Gurenko A. and Bischoff A. (2014) Tracking aqueous alteration of CM chondrites—Insight from in-situ oxygen isotope measurements of calcite. *Lunar Planet. Sci. 45*. Lunar Planet. Inst., Houston. #1761 (abstr.).

Howard K. T., Alexander C. M. O., Schrader D. L. and Dyl K. A. (2015) Classification of hydrous meteorites (CR, {CM} and {C2} ungrouped) by phyllosilicate fraction: PSD-XRD modal mineralogy and planetesimal environments. *Geochim. Cosmochim. Acta* **149**, 206–222.

Howard K. T., Benedix G. K., Bland P. A. and Cressey G. (2009) Modal mineralogy of CM2 chondrites by X-ray diffraction (PSD-XRD). Part 1: Total phyllosilicate abundance and the degree of aqueous alteration. *Geochim. Cosmochim. Acta* **73**, 4576–4589.

Johnson C. A. and Prinz M. (1993) Carbonate compositions in CM and CI chondrites and implications for aqueous alteration. *Geochim. Cosmochim. Acta* **57**, 2843–2852.

Ketcham R. A. (2005a) Computational methods for quantitative analysis of three-dimensional features in geological specimens. *Geospherei. 1*, 32-41.

Ketcham R. A. (2005b) Three-dimensional grain fabric measurements using high-resolution X-ray computed tomography. *J. Struct. Geol.* **27**, 1217–1228.

Kurat G., Koeberl C., Presper T., Brandstätter F. and Maurette M. (1994) Petrology and geochemistry of Antarctic micrometeorites. *Geochim. Cosmochim. Acta* **58**, 3879–

3904.

Lécuyer C., Hutzler A., Amiot R., Daux V., Grosheny D., Otero O., Martineau F., Fourel F., Balter V. and Reynard B. (2012) Carbon and oxygen isotope fractionations between aragonite and calcite of shells from modern molluscs. *Chem. Geol.* **332**–**333**, 92–101.

Lee M. R. and Ellen R. (2008) Aragonite in the Murray (CM2) carbonaceous chondrite: implications for parent body compaction and aqueous alteration. *Meteorit. Planet. Sci.* **43**, 1219–1231.

Lee M. R., Lindgren P. and Sofe M. R. (2014) Aragonite, breunnerite, calcite and dolomite in the CM carbonaceous chondrites: High fidelity recorders of progressive parent body aqueous alteration. *Geochim. Cosmochim. Acta* **144**, 126–156.

Lee M. R., Lindgren P., Sofe M. R., Alexander C. M. O. and Wang J. (2012) Extended chronologies of aqueous alteration in the CM2 carbonaceous chondrites: Evidence from carbonates in Queen Alexandra Range 93005. *Geochim. Cosmochim. Acta* **92**, 148–169.

Lee M. R., Sofe M. R., Lindgren P., Starkey N. A. and Franchi I. A. (2013) The oxygen isotope evolution of parent body aqueous solutions as recorded by multiple carbonate generations in the Lonewolf Nunataks 94101 CM2 carbonaceous chondrite. *Geochim. Cosmochim. Acta* **121**, 452–466.

Lindgren P., Hanna R. D., Dobson K. J., Tomkinson T. and Lee M. R. (2015) The paradox between low shock-stage and evidence for compaction in CM carbonaceous chondrites explained by multiple low-intensity impacts. *Geochim. Cosmochim. Acta* **148**, 159–178.

Lindgren P., Lee M. R., Sofe M. and Burchell M. J. (2011) Microstructure of calcite in the CM2 carbonaceous chondrite LON 94101: Implications for deformation history during and/or after aqueous alteration. *Earth Planet. Sci. Lett.* **306**, 289–298.

Lindgren P., Lee M. R., Sofe M. R. and Zolensky M. E. (2013) Clasts in the CM2 carbonaceous chondrite Lonewolf Nunataks 94101: Evidence for aqueous alteration prior to complex mixing. *Meteorit. Planet. Sci.* **48**, 1074–1090.

Lindgren P., Lee M. R., Starkey N. A. and Franchi I. A. (2017) Fluid evolution in CM carbonaceous chondrites tracked through the oxygen isotopic compositions of carbonates. *Geochim. Cosmochim. Acta* **204**, 240–251.

Luo W. and Wang S. (2009) Transmission of δ 13C signals and its paleoclimatic implications in Liangfeng Cave system of Guizhou Province, SW China. *Environ. Earth Sci.* **59**, 655–661.

Marrocchi Y., Bekaert D. V. and Piani L. (2018) Origin and abundance of water in carbonaceous asteroids. *Earth Planet. Sci. Lett.* **482**, 23–32.

Marrocchi Y., Gounelle M., Blanchard I., Caste F. and Kearsley A. T. (2014) The Paris CM chondrite: Secondary minerals and asteroidal processing. *Meteorit. Planet. Sci.* **49**, 1232–1249.

Martin P. M. and Mills A. A. (1980) Preferred chondrule orientations in meteorites. *Earth Planet. Sci. Lett.* **51**, 18–25.

McSween H. Y. (1979) Are carbonaceous chondrites primitive or processed? A review. *Rev. Geophys.* **17**, 1059–1078.

Metzler K., Bischoff A. and Stöffler D. (1992) Accretionary dust mantles in CM chondrites: Evidence for solar nebula processes. *Geochim. Cosmochim. Acta* **56**, 2873–2897.

Mook W. G., Bommerson J. C. and Staverman W. H. (1974) Carbon isotope fractionation between dissolved bicarbonate and gaseous carbon dioxide. *Earth Planet. Sci. Lett.* **22**, 169–176.

Morbidelli A., Bitsch B., Crida A., Gounelle M., Guillot T., Jacobson S., Johansen A., Lambrechts M and Lega E. (2016) Fossilized condensation lines in the Solar System protoplanetary disk. *Icarus* **267**, 368–376.

Nakamura T. (2000) Impact-Induced Textural Changes of CV Carbonaceous Chondrites: Experimental Reproduction. *Icarus* **146**, 289–300.

Nakamura T. (2005) Post-hydration thermal metamorphism of carbonaceous chondrites. *J. Mineral. Petrol. Sci.* **100**, 260–272.

Nakamura T., Tomeoka K., Sekine T. and Takeda H. (1995) Impact-induced chondrule flattening in the Allende CV3 carbonaceous chondrite: Shock experiments. *Meteorit. Planet. Sci.* **30**, 344–347.

Nakamura T., Tomeoka K. and Takeda H. (1992) Shock effects of the Leoville CV carbonaceous chondrite: a transmission electron microscope study. *Earth Planet. Sci. Lett.* **114**, 159–170.

Nakato A., Nakamura T., Kitajima F. and Noguchi T. (2008) Evaluation of dehydration mechanism during heating of hydrous asteroids based on mineralogical and chemical analysis of naturally and experimentally heated CM chondrites. *Earth Planets Space* **60**, 855–864.

Palmer E. E. and Lauretta D. S. (2011) Aqueous alteration of kamacite in CM chondrites. *Meteorit. Planet. Sci.* **46**, 1587–1607.

Pignatelli I., Mugnaioli E. and Marrocchi Y. (2018) Cronstedtite polytypes in the Paris meteorite. *European Journal of Mineralogy*. DOI: 10.1127/ejm/2018/0030-2713.

Pignatelli I., Marrocchi Y., Mugnaioli E., Bourdelle F. and Gounelle M. (2017) Mineralogical, crystallographic and redox features of the earliest stages of fluid alteration in CM chondrites. *Geochim. Cosmochim. Acta* **209**, 106–122.

Pignatelli I., Marrocchi Y., Vacher L. G., Delon R. and Gounelle M. (2016) Multiple precursors of secondary mineralogical assemblages in CM chondrites. *Meteorit. Planet. Sci.* **51**, 785–805.

Proskurowski G. (2010) Abiogenic hydrocarbon production at the geosphere–biosphere interface via serpentinization reactions. In: Timmis, K.N., McGenity, T., van der

Meer, J.R., de Lorenzo, V. (Eds.), Handbook of Hydrocarbon and Lipid Microbiology. Springer, Berlin Heidelberg, pp. 215-231.

Riciputi L. R., McSween H. Y., Johnson C. A. and Prinz M. (1994) Minor and trace element concentrations in carbonates of carbonaceous chondrites, and implications for the compositions of coexisting fluids. *Geochim. Cosmochim. Acta* **58**, 1343–1351.

Rollion-Bard C., Mangin D. and Champenois M. (2007) Development and application of oxygen and carbon isotopic measurements of biogenic carbonates by ion microprobe. *Geostand. Geoanalytical Res.* **31**, 39–50.

Rubin A. E. (2015) An American on Paris: extent of aqueous alteration of a CM chondrite and the petrography of its refractory and amoeboid olivine inclusions. *Meteorit. Planet. Sci.* **50**, 1595–1612.

Rubin A. E. (2012) Collisional facilitation of aqueous alteration of CM and CV carbonaceous chondrites. *Geochim. Cosmochim. Acta* **90**, 181–194.

Rubin A. E. and Ma C. (2017) Meteoritic minerals and their origins. *Chem. Erde - Geochem.* **77**, 325-385.

Rubin A. E. and Swindle T. D. (2011) Flattened chondrules in the LAP 04581 LL5 chondrite: Evidence for an oblique impact into LL3 material and subsequent collisional heating. *Meteorit. Planet. Sci.* **46**, 587–600.

Rubin A. E., Trigo-Rodríguez J. M., Huber H. and Wasson J. T. (2007) Progressive aqueous alteration of CM carbonaceous chondrites. *Geochim. Cosmochim. Acta* **71**, 2361–2382.

Rubin A. E. and Wasson J. T. (1986) Chondrules in the Murray CM2 meteorites and compositional differences between CM-CO and ordinary chondrite chondrules. *Geochim. Cosmochim. Acta* **50**, 307–315.

Scott E. R. D., Keil K. and Stöffler D. (1992) Shock metamorphism of carbonaceous chondrites. *Geochim. Cosmochim. Acta* **56**, 4281–4293.

Scott E. R. D. and Taylor G. J. (1983) Chondrules and other components in C, O, and E chondrites: Similarities in their properties and origins. *J. Geophys. Res. Solid Earth* **88**, B275–B286.

Sephton M. A. and Botta O. (2005) Recognizing life in the Solar System: guidance from meteoritic organic matter. *Int. J. Astrobiol.* **4**, 269–276.

Sofe M. (2013) The oldest carbonate minerals on Earth: Insights into the early history of the Solar System. Ph. D. thesis, Univ. Glasgow.

Sneyd D. S., McSween H. Y., Sugiura N., Strangway D. W. and Nord G. L. (1988) Origin of Petrofabrics and Magnetic Anisotropy in Ordinary Chondrites. *Meteoritics* **23**, 139–149.

Stiller M., Rounick J. S. and Shasha S. (1985) Extreme carbonisotope enrichments in evaporating brines. *Nature* **316**, 434–435.

967 Stöffler D., Keil K. and R.D S. E. (1991) Shock metamorphism of ordinary chondrites.
968 *Geochim. Cosmochim. Acta* **55**, 3845–3867.

969 Suavet C., Alexandre A., Franchi I. A., Gattacceca J., Sonzogni C., Greenwood R. C., Folco
970 L. and Rochette P. (2010) Identification of the parent bodies of micrometeorites with
971 high-precision oxygen isotope ratios. *Earth Planet. Sci. Lett.* **293**, 313–320.

972 Suttle M. D., Genge M. J. and Russell S. S. (2017) Shock fabrics in fine-grained
973 micrometeorites. *Meteorit. Planet. Sci.* **52**, 2258–2274.

974 Telus M., Alexander C. M. O'D., Wang J. and Hauri E. H. (2017) In situ analyses of
975 carbonate and magnetite in CM1 chondrites. *Lunar Planet. Sci. 48*. Lunar Planet. Inst.,
976 Houston. #1725 (abstr.).

977 Tomeoka K. and Buseck P. R. (1985) Indicators of aqueous alteration in CM carbonaceous
978 chondrites: Microtextures of a layered mineral containing Fe, S, O and Ni. *Geochim.*
979 *Cosmochim. Acta* **49**, 2149–2163.

980 Tomeoka K., Yamahana Y. and Sekine T. (1999) Experimental shock metamorphism of the
981 Murchison CM carbonaceous chondrite. *Geochim. Cosmochim. Acta* **63**, 3683–3703.

982 Tyra M. A., Farquhar J., Guan Y. and Leshin L. A. (2012) An oxygen isotope dichotomy in
983 CM2 chondritic carbonates—A SIMS approach. *Geochim. Cosmochim. Acta* **77**, 383–
984 395.

985 Tyra M. A., Farquhar J., Wing B. A., Benedix G. K., Jull A. J. T., Jackson T. and Thiemens
986 M. H. (2007) Terrestrial alteration of carbonate in a suite of Antarctic CM chondrites:
987 Evidence from oxygen and carbon isotopes. *Geochim. Cosmochim. Acta* **71**, 782–795.

988 Tyra M., Brearley A. and Guan Y. (2016) Episodic carbonate precipitation in the CM
989 chondrite ALH 84049: An ion microprobe analysis of O and C isotopes. *Geochim.*
990 *Cosmochim. Acta* **175**, 195–207.

991 Vacher L. G., Marrocchi Y., Verdier-Paoletti M. J., Villeneuve J. and Gounelle M. (2016)
992 Inward radial mixing of interstellar water ices in the solar protoplanetary disk.
993 *Astrophys. J.* **827**, L1.

994 Vacher L. G., Marrocchi Y., Villeneuve J., Verdier-Paoletti M. J. and Gounelle M. (2017)
995 Petrographic and C & O isotopic characteristics of the earliest stages of aqueous
996 alteration of CM chondrites. *Geochim. Cosmochim. Acta* **213**, 271–290.

997 Verdier-Paoletti M. J., Marrocchi Y., Avice G., Roskosz M., Gurenko A. and Gounelle M.
998 (2017a) Oxygen isotope constraints on the alteration temperatures of CM chondrites.
999 *Earth Planet. Sci. Lett.* **458**, 273–281.

1000 Verdier-Paoletti M. J., Vacher L. G., Marrocchi Y., Gattacceca J., Sonzogni C., Gurenko A.
1001 and Gounelle M. (2017b) Teting the genetic relationship between fluid alteration and
1002 brecciation: the case of Boriskino. In *80th Annual Meeting of the Meteoritical Society*.
1003 #6081 (abstr.).

1004 Watt L. E., Bland P. A., Prior D. J. and Russell S. S. (2006) Fabric analysis of Allende matrix
1005 using EBSD. *Meteorit. Planet. Sci.* **41**, 989–1001.

White S. N. (2009) Laser Raman spectroscopy as a technique for identification of seafloor hydrothermal and cold seep minerals. *Chem. Geol.* **259**, 240–252.

Woodcock N. H. and Naylor M. (1983) Randomness testing in three-dimensional orientation data. *J. Struct. Geol.* **5**, 539–548.

Zolensky M. E., Mittlefehldt D. W., Lipschutz M. E., Wang M.-S., Clayton R. N., Mayeda T. K., Grady M. M., Pillinger C. and B D. (1997) CM chondrites exhibit the complete petrologic range from type 2 to 1. *Geochim. Cosmochim. Acta* **61**, 5099–5115.

Zolotov M. Y. (2014) Formation of brucite and cronstedtite-bearing mineral assemblages on Ceres. *Icarus* **228**, 13–26.

FIGURE CAPTIONS

Figure 1: (a) Full 3D volume rendering of the bulk sample of Boriskino using X-ray computed tomography (XCT). The dashed line represents the location of (b). (b) XCT slice #1005 from the full volume. The elliptical dark-toned objects are interpreted as type I chondrules.

Figure 2: Back-scattered electron (BSE) mosaics of the two polished sections of the CM2 Boriskino (sections #3 & #4). (a) BSE mosaic of Boriskino section #3 in which the different lithologies are marked (numbered white circles) and delimited (dashed lines). Analyzed Type1a aragonites are represented by green diamonds, Type 1a calcites by green points, Type 2a calcites by red circles and calcite veins by purple triangle. (b) BSE mosaic of Boriskino section #4 in which Ca-carbonate grains and different lithologies are indicated and outlined. The arbitrary orientation of two sections used for petrofabric determination is represented by the axis at the bottom left of the figure (the horizontal = 0°).

Figure 3: BSE mosaics of delimited regions of the three lithologies in section #4. (a) BSE mosaic of lithology 1 (number in white circle) in contact with lithology 2 (delimited by the dashed line). The Type 2a calcite grain is outlined with a red dashed line. Sph: sulphide, Phy: phyllosilicate. (b) BSE mosaic of lithology 2 in contact with lithology 1. (c) BSE mosaic of a specific region of lithology 3 in contact with lithology 1 and other lithologies. The Type 1a aragonite grains are represented by green diamonds.

Figure 4: (a) BSE image of Type 1a aragonite (A) surrounded by a fine rim of phyllosilicate (Phy) in lithology 3 (white circle, #4). (b) BSE image of Type 1a calcite (C) surrounded by a

fine rim of phyllosilicate in lithology 3 (#4). (c) BSE image of polycrystalline aggregates of Type 2 calcite (C), exhibiting phyllosilicate (Phy) and sulphide (Sph), located in the matrix of lithology 1 (#3). (d) BSE image of a calcite vein, hundreds of micrometers in length and ten of micrometers in width, in lithology 1 (#3). The large white arrows indicate the mean orientations of the petrofabrics of the three lithologies in section #4 as determined in Fig. 7b, 7c and 7d. The holes on the Fig. a-c show positions of ion probe spots.

Figure 5: (a) Oxygen three-isotope plot for Type 1a aragonite (green diamonds), Type 1a calcite (green circles), Type 2a calcite (red circles) and the calcite vein (purple triangle) from this study (errors are given in 2σ). The dashed line represents the linear regression of our dataset ($\delta^{17}O = 0.62$ (± 0.05, 2σ) x $\delta^{18}O - 4.3$ (± 1.3, 2σ)). The black star denotes the mean O-isotopic composition of CM anhydrous silicates (Anhydrous silicate[1]: Clayton and Mayeda, 1984). (b) $\Delta^{17}O$ *vs* $\delta^{18}O$ plot of the populations 1 (green points) and 2 (red and purple points) of Ca-carbonates. $\Delta^{17}O$ represents the deviation from the TFL: $\Delta^{17}O = \delta^{17}O - 0.52 \times \delta^{18}O$. The O-isotopic compositions of the two populations are represented by the grey square (population 1) and the white and grey square (population 2). TFL: Terrestrial Fractionation Line, $\delta^{17}O = 0.52 \times \delta^{18}O$. CMW: CM Water line, $\delta^{17}O = 0.69 \times \delta^{18}O - 2.12$ (Verdier-Paoletti et al., 2017a). CCAM: Carbonaceous Chondrite Anhydrous Mineral line, $\delta^{17}O = 0.94 \times \delta^{18}O - 4.2$.

Figure 6: $\delta^{13}C$ values of Type 1a aragonite (green diamonds), Type 1a calcite (green circles) and Type 2a calcite (red circles) from this study (errors are given in 2σ). The mean values of the Type 1 and Type 2 Ca-carbonates are represented by the green and the red square, respectively. The *in situ* data from the literature (grey circles) are also shown in the figure (CM2.7 Paris[1]: Vacher et al., 2017; CM2.5 Murchison[2]: Fujiya et al., 2015; CM2.2-2.3

Nogoya[3]: Fujiya et al., 2016; CM1 ALH 83100[4], ALH 84034[4], MET 01070[4]: Telus et al., 2017; CM1 ALH 84049[5]: Tyra et al., 2016).

Figure 7: a) BSE image of Type 2a polycrystalline calcite (C) grains located in a flattened chondrule surrounded by a fine-grained rim (FGR) and accompanied by phyllosilicate (Phy) and sulphide inclusions (Sph) in lithology 2. The solid white line represents the direction of the long axis of the fitted chondrule ellipse. The double white arrow indicates the mean orientation of the petrofabric of this lithology. b) BSE image of another example of Type 2a polycrystalline calcite (C) grains located in a flattened chondrule in lithology 1 (section #3). c) BSE image of a squeezed type I chondrule located in lithology 1 (section #4). The red dashed line delimits a Type 2a polycrystalline grain located in the matrix. The matrix that surrounds the squeezed chondrule is accompanied by numerous patches of phyllosilicate (Phy) and sulphide (Sph) grains.

Figure 8: Histograms showing the deviation of particles (i.e., chondrule, TCI clump and olivine grain) from the median azimuth of each lithology according to the method of Rubin (2012). The blue area represents the Gaussian fits ($y = a \times e^{\left(\frac{x-b}{c}\right)^2}$) of the data set. (a) Lithology 1 in section 3 (#3) has a strong peak near the median azimuth materialized by a high maximum frequency (a = 24%), a low standard deviation (c = 20.5°) and 46% of the particles within 10° of the median azimuth angle (R^2 of the Gaussian fit = 0.98). The solid purple lines and the black dashed lines indicate the mean orientations of the calcite veins and the fractures, respectively identified in this lithology. The solid black line corresponds to the median azimuth value normalized to 0° using the Rubin (2012) method. (b) Lithology 1 in section 4 (#4) has a weak peak near the median azimuth revealed by an intermediate maximum frequency (a = 13%), an intermediate standard deviation (c = 27°) and 26% of the

particles within 10° of the median azimuth angle (R^2 of the Gaussian fit = 0.63). The solid black line corresponds to the median azimuth value normalized to 0°, but for comparing the mean directions of the three lithologies in section 4, the mean direction values determined from the orientation of the section (see Fig. 2) are indicated. (c) Lithology 2 in section 4 (#4) also has weak peak near the median azimuth demonstrated by a low maximum frequency (a = 10%), a high standard deviation (c = 34°) and 21% of the particles within 10° of the median azimuth angle (R^2 of the Gaussian fit = 0.48). (d) Lithology 3 in section 4 (#4) has a strong peak near the median azimuth confirmed by a high maximum frequency (a = 22%), a low standard deviation (c = 21°) and 41% of the particles within 10° of the median azimuth angle (R^2 of the Gaussian fit = 0.98).

Figure 9: Orientation plot of fitted ellipsoid from bulk X-ray computed tomography analyses of a type I chondrule in Boriskino. (a) Projection of the primary axes (R1) of the fitted ellipsoid (black circles) and the mean value (V1) and pole value (V3) of the data set (red diamonds). The blue color gradient represents the density contour values of the data set. C = the strength parameter, K = the shape parameter and n = the number of extracted objects. (b) Projection of the tertiary axes (R3) of the fitted ellipsoid (black circles) and the mean value (V1) and pole value (V3) of the data set (blue diamonds). The red color gradient represents the density contour values of the data set.

Figure 10: Schematic diagram representing the main processes controlling the oxygen isotopic compositions of Ca-Carbonates. The main trend, with a slope in the range 0.62-0.70 (dashed line, see text), results from O-isotopic exchange between ^{17,18}O-rich CM primordial water (blue point, Fujiya, 2018) and anhydrous silicates (black star, Clayton and Mayeda, 1984). For a fluid with a given Δ^{17}O value, a thermal gradient can occur during carbonate

precipitation, generating a shift of carbonate O-isotopic compositions along a slope of 0.52 for a given degree of isotopic exchange**.** TFL: Terrestrial Fractionation Line, CCAM: Carbonaceous Chondrite Anhydrous Mineral line.

Figure 11: Relationship between intensity of a *single* shock pressure and mean chondrule aspect ratio in an experimental shock on the CM Murchison[1] (solid black line and white circle; Tomeoka et al., 1999) and on the CV Allende[2] (black dotted line and black circle; Nakamura et al., 2000). The mean X-ray computed tomography (XCT) aspect ratio of the Boriskino type I chondrules (yellow square) and Murchison[3] dark-toned XCT objects (purple square; Hanna et al., 2015) is reported on the CV and CM trends. The light grey rectangle that cuts the CM trend represents the end of the correlation and the effects of the CM shock experiments above 30 GPa (Tomeoka et al., 1999).

Figure 12: Relationship between degree of alteration *vs* percentage of particles with long axes within 10° of the median azimuth. Data from the lithology 1, 2 and 3 are represented by red circles, red square and green circle, respectively. Data and associated correlation from Rubin (2012) are shown in blue circles and black dashed line, respectively. Percentages of chondrules alignment with long axis within 10° from Lindgren et al. (2015) are also represented (yellow circles).

Figure 13: (a) BSE image showing an interpreted pre-deformation Type 1a Ca-carbonate (CC) grain isolated in the matrix and a stretched phyllosilicate (Phy), set in the petrofabric of lithology 3 (section #4). The double white arrows represent the deformation of the matrix around the Ca-carbonate grain, as highlighted by the elongation of the phyllosilicate. (b) BSE

image of stretched clumps of phyllosilicates (Phy) and elongate sulphide (Sph) grains parallel to the petrofabric of lithology 3 (#4).

Figure 14: Schematic representation of the thermal and deformation history of the CM parent body and the expected locations of the Boriskino lithologies at different times. (a) t_1: precipitation of the Type 1a calcite and aragonite of lithology 3 by the decay of the ^{26}Al. (b) t_2: formation of fractures and cracks by high intensity impact(s). (c) t_3: circulation of fluid flow within the newly formed fractures in lithologies 1 and 2. (d) t_4: release and mixing of Boriskino's clasts from the CM parent body by a new set of low intensity impact(s).

Figure 15: $\delta^{13}C$ *vs.* $\delta^{18}O$ values for Type 1a aragonite (green diamonds), Type 1a calcite (green circles) and Type 2a calcite (red circles) from this study (errors are given in 2σ). We also show the *in situ* $\delta^{13}C$-$\delta^{18}O$ data of the Type 1 (light grey circles) and Type 2 (dark grey circles) calcite from the CM2.2-2.3 Nogoya[1] (Fujiya et al., 2016). Because of the large amount of data, the ranges of Ca-carbonate $\delta^{13}C$-$\delta^{18}O$ values reported by Fujiya et al. (2015), Fujiya et al. (2016), Telus et al. (2017) and Vacher et al. (2017) are shown as light grey (CM2) and dark grey (CM1) areas for simplicity. The $\delta^{13}C$-$\delta^{18}O$ values of the CM1 MET 01070 have also been isolated from the literature dataset by black dashed lines (Telus et al., 2017). The $\delta^{13}C$-$\delta^{18}O$ values of CC6, CC7, CC8 and CC15 grains are given as mean values and errors associated were calculated using the error propagation law.

Figure 16: (a) $\delta^{13}C$ *vs.* $\delta^{18}O$ values for Type 1a aragonite (green diamonds), Type 1a calcite (green circles) and Type 2a calcite (red circles) from this study (errors are given in 2σ). The grey squares represent the *in situ* $\delta^{13}C$-$\delta^{18}O$ data of the Type 1 Ca-carbonates in the CM2.5 Murchison[1] (Fujiya et al., 2015) and CM2.7 Paris[1] (Vacher et al., 2017). We also show the *in*

situ $\delta^{13}C$-$\delta^{18}O$ data of the Type 1 (light grey circles) and Type 2 (dark grey circles) calcite from the CM2.2-2.3 Nogoya[1] (Fujiya et al., 2016). The white triangle lines represent the predicted isotopic compositions of CM carbonates as a function of temperature and the mole fraction of CO_2 in a CO-CO_2-H_2O system ($\delta^{13}C_{CO}$ = -5‰ and $\delta^{18}O_{H2O}$ = 5‰) (CO-CO_2 gas[1]: Alexander et al., 2015). The white triangles on the model mark 10°C intervals. The blue rectangle represents the predicted range of $\delta^{13}C$-$\delta^{18}O$ values of Ca-carbonates that precipitated from varying equilibration between $^{17,18}O$-rich water with ^{12}C- and ^{13}C-rich soluble organic matter at 110°C (Vacher et al., 2017). The $\delta^{13}C$-$\delta^{18}O$ values of CC6, CC7, CC8 and CC15 grains are given as mean values and errors associated were calculated using the error propagation law. (b) $\delta^{13}C$ *vs.* $\delta^{18}O$ values of the Type 2a calcite (red circles) from this study and Type 1 (light grey circles) and Type 2 (dark grey circles) calcite from the CM Nogoya[2] (Fujiya et al., 2016) (errors are given in 2σ). The grey dashed line represents the initial $\delta^{13}C_{HCO_{3_0}^-}$ value of the fluid used in the Rayleigh distillation calculations (see Eq.(2), $\delta^{13}C_{HCO_{3_0}^-} = 30‰$). Percent estimates of dissolved carbon escape from the fluid by Rayleigh distillation are also shown for a mean temperature of 110°C. The $\delta^{13}C$-$\delta^{18}O$ values of CC6 and CC8 grains are given as mean values and errors associated were calculated using the error propagation law.

1187 **FIGURES**

1188

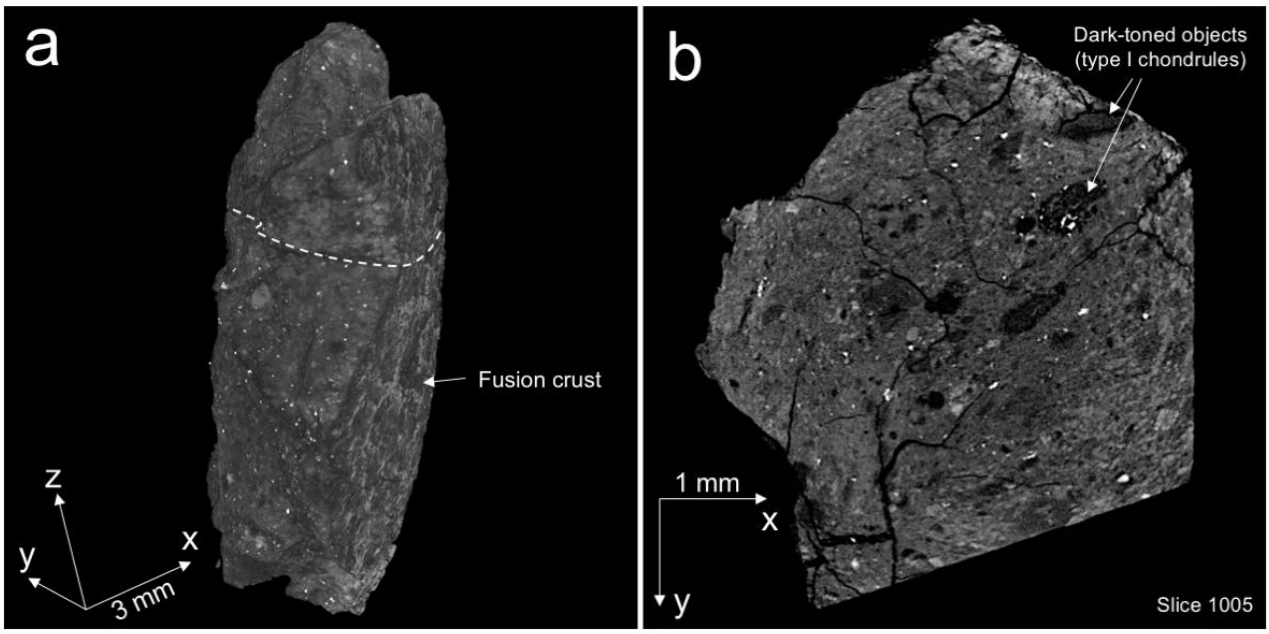

1189

1190 **Figure 1**

1191

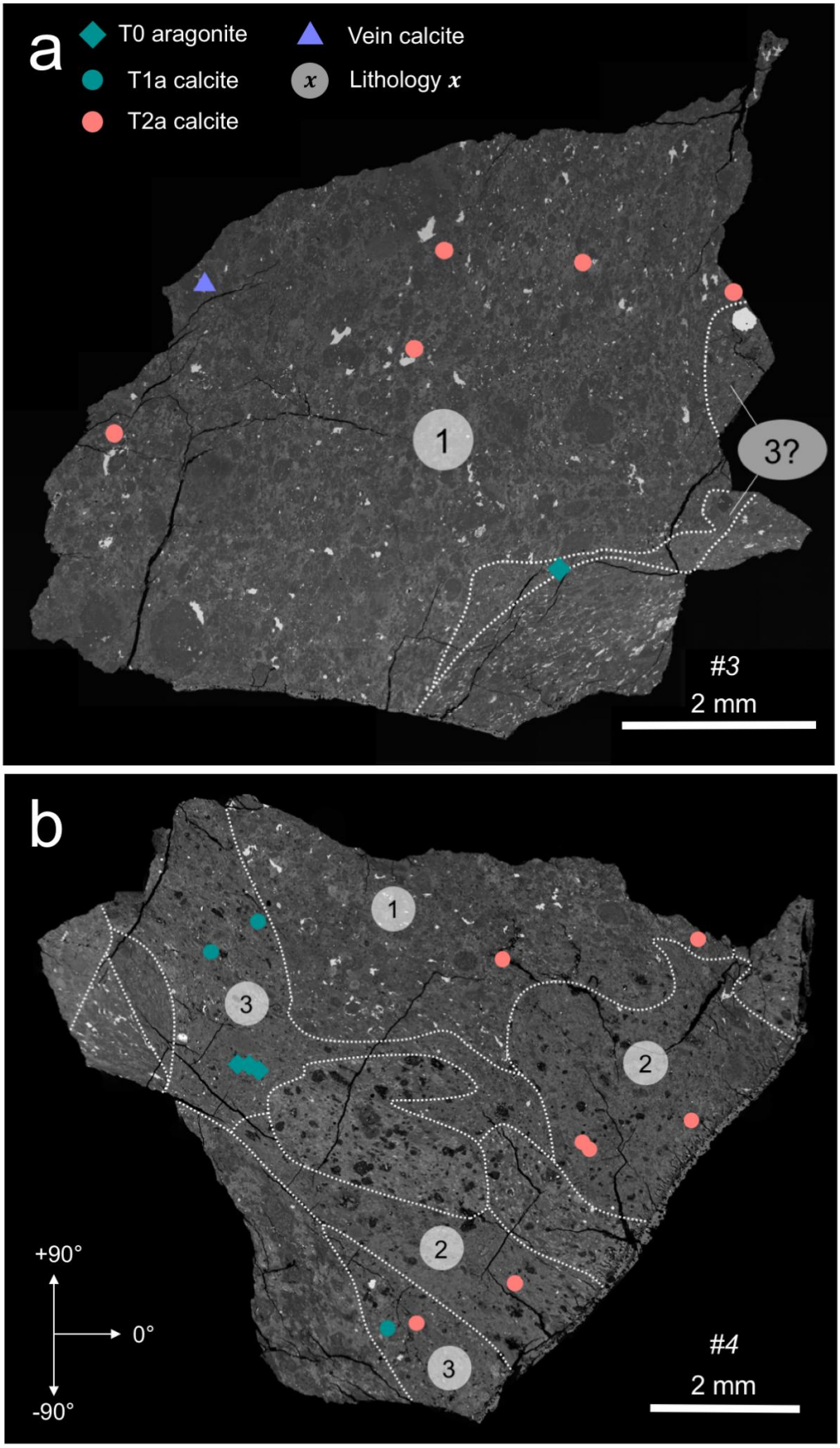

1192

1193 **Figure 2**

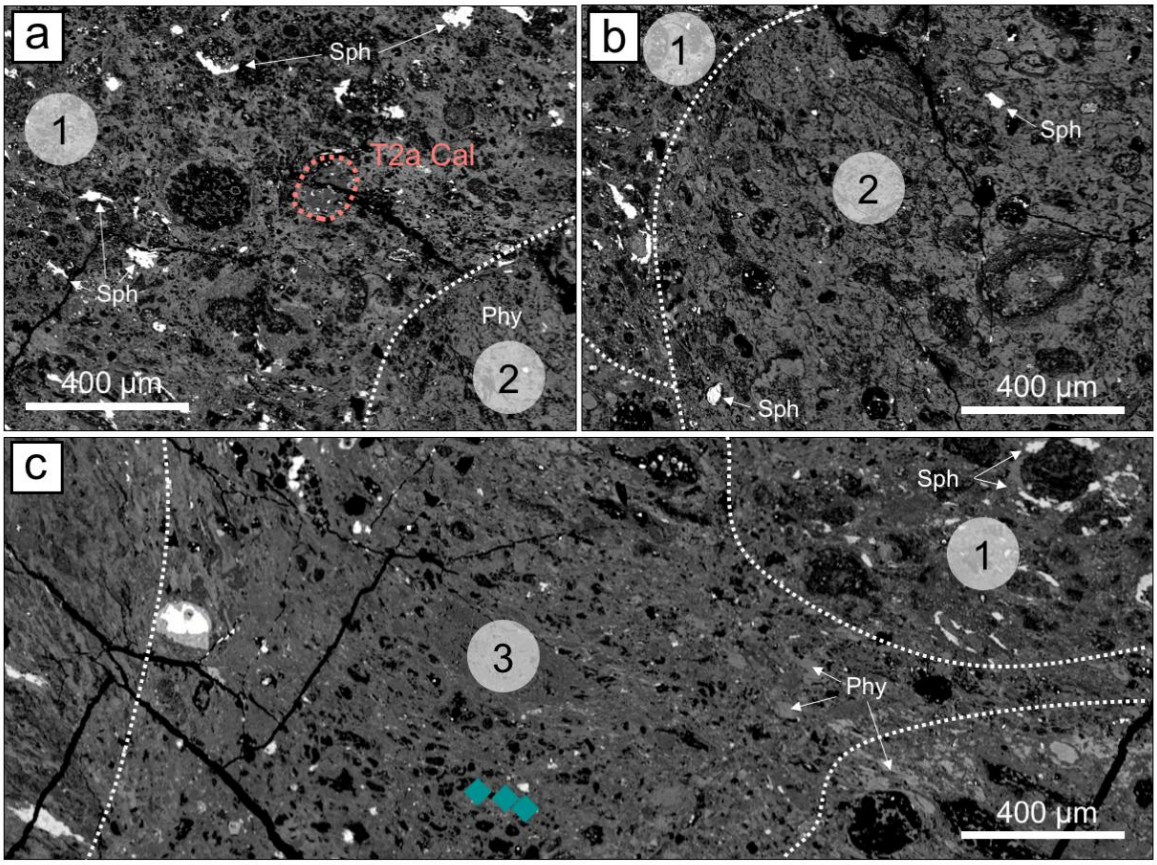

1194

1195 **Figure 3**

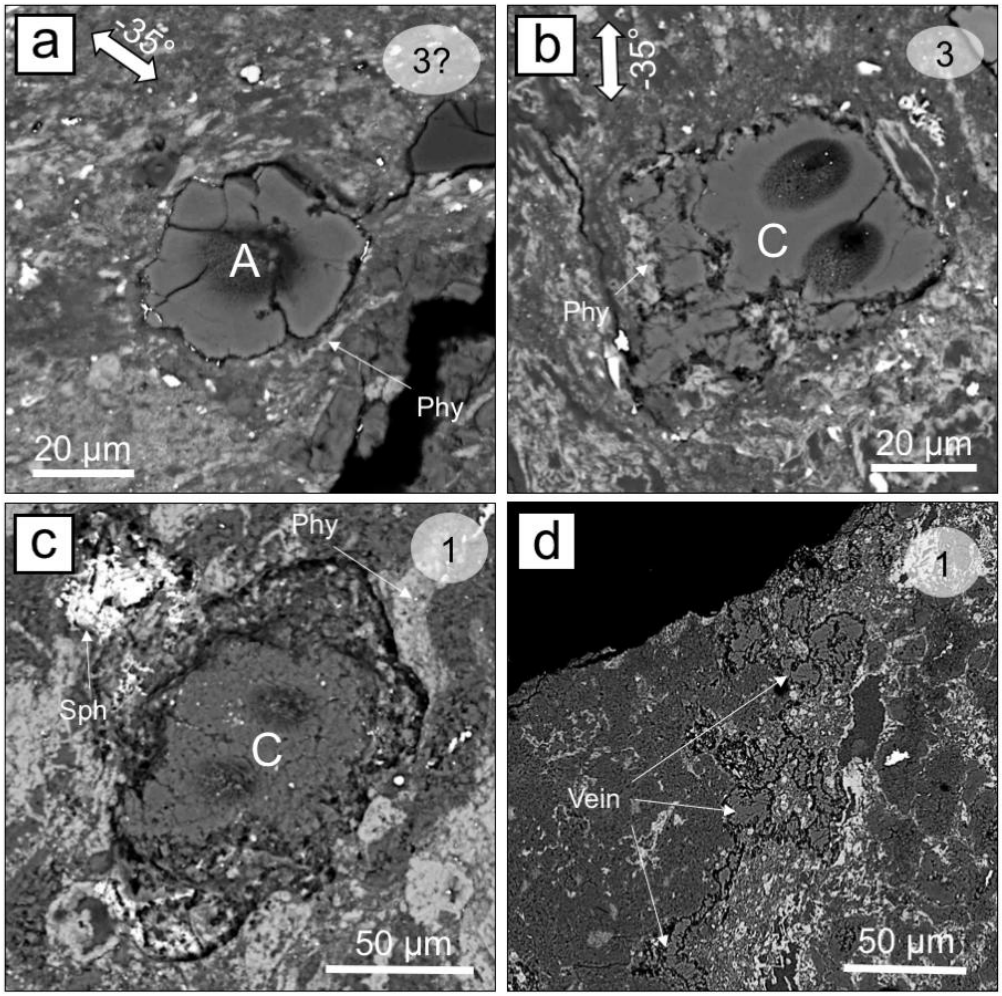

1196

1197 **Figure 4**

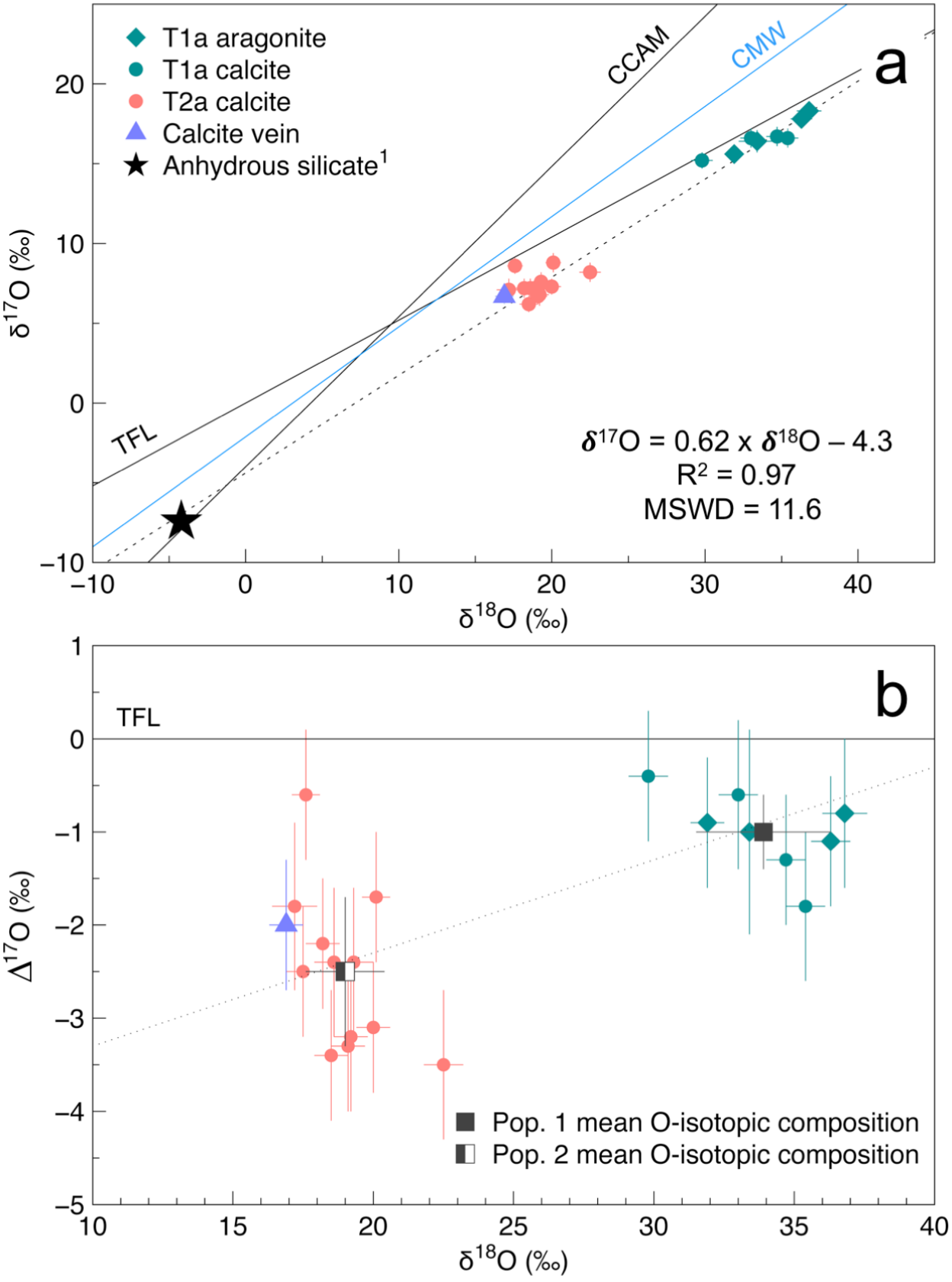
T1a aragonite
T1a calcite
T2a calcite
Calcite vein
Anhydrous silicate[1]
CCAM
CMW
a
TFL
δ17O = 0.62 x δ18O – 4.3
R2 = 0.97
MSWD = 11.6
δ17O (‰)
δ18O (‰)
b
TFL
Pop. 1 mean O-isotopic composition
Pop. 2 mean O-isotopic composition
Δ17O (‰)
δ18O (‰)

Figure 5

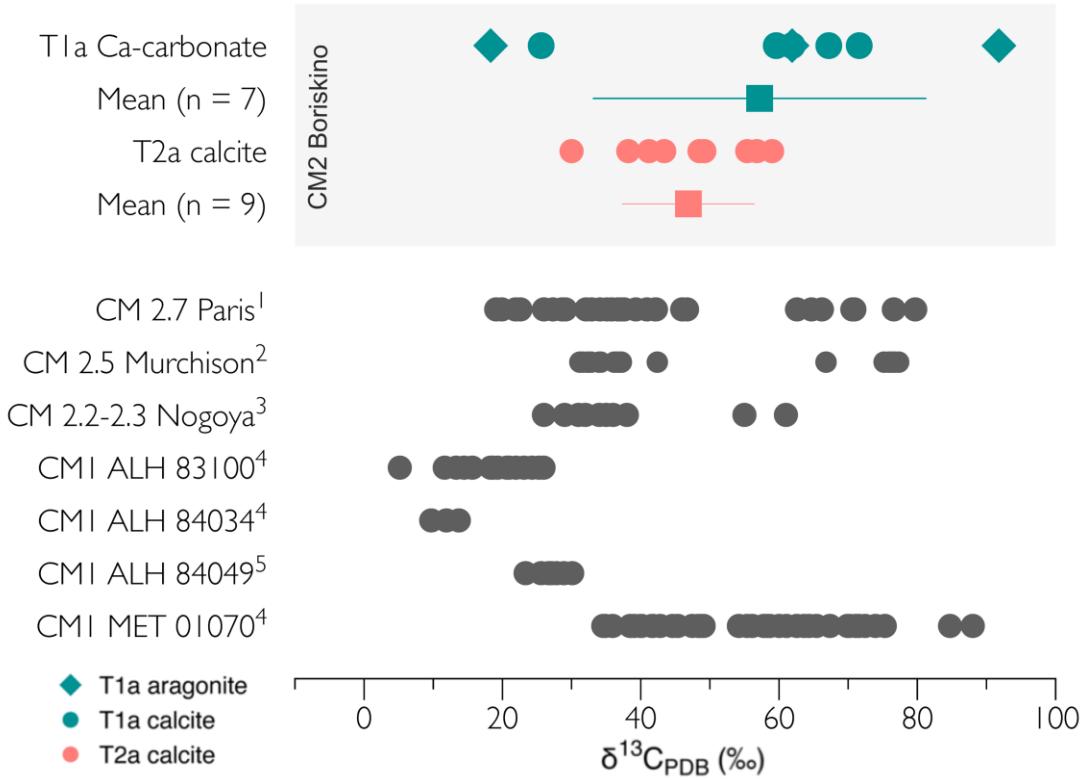
T1a Ca-carbonate
Mean (n = 7)
T2a calcite
Mean (n = 9)
CM2 Boriskino
CM 2.7 Paris[1]
CM 2.5 Murchison[2]
CM 2.2-2.3 Nogoya[3]
CM1 ALH 83100[4]
CM1 ALH 84034[4]
CM1 ALH 84049[5]
CM1 MET 01070[4]
T1a aragonite
T1a calcite
T2a calcite
0
20
40
60
80
100
δ13CPDB (‰)

Figure 6

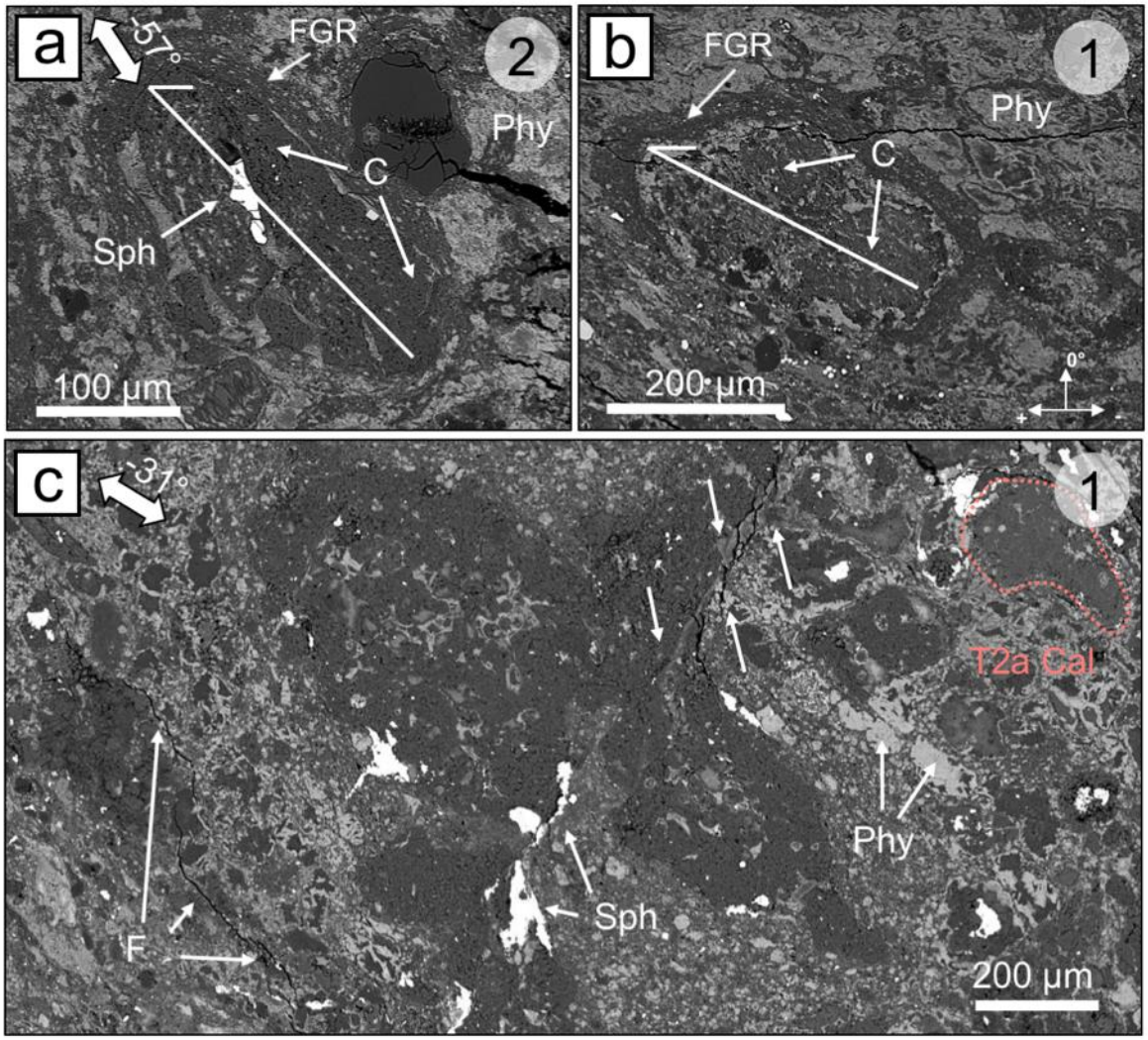
a
51°
FGR
2
Phy
C
Sph
100 µm
b
FGR
1
Phy
C
200 µm
0°
c
37°
1
T2a Cal
Phy
Sph
F
200 µm

Figure 7

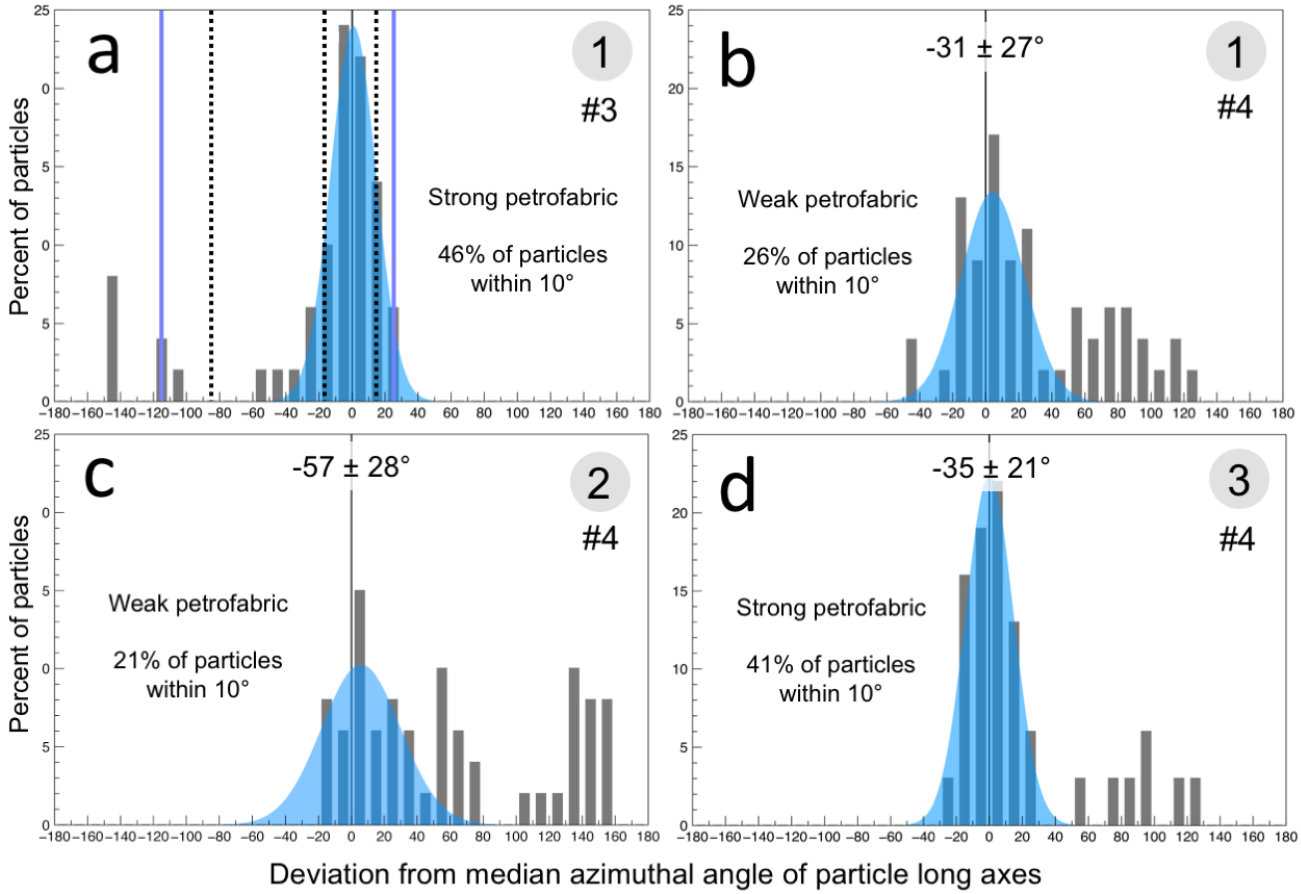
a
1
#3
Strong petrofabric
46% of particles
within 10°
b
-31 ± 27°
1
#4
Weak petrofabric
26% of particles
within 10°
c
-57 ± 28°
2
#4
Weak petrofabric
21% of particles
within 10°
d
-35 ± 21°
3
#4
Strong petrofabric
41% of particles
within 10°
Percent of particles
Deviation from median azimuthal angle of particle long axes

Figure 8

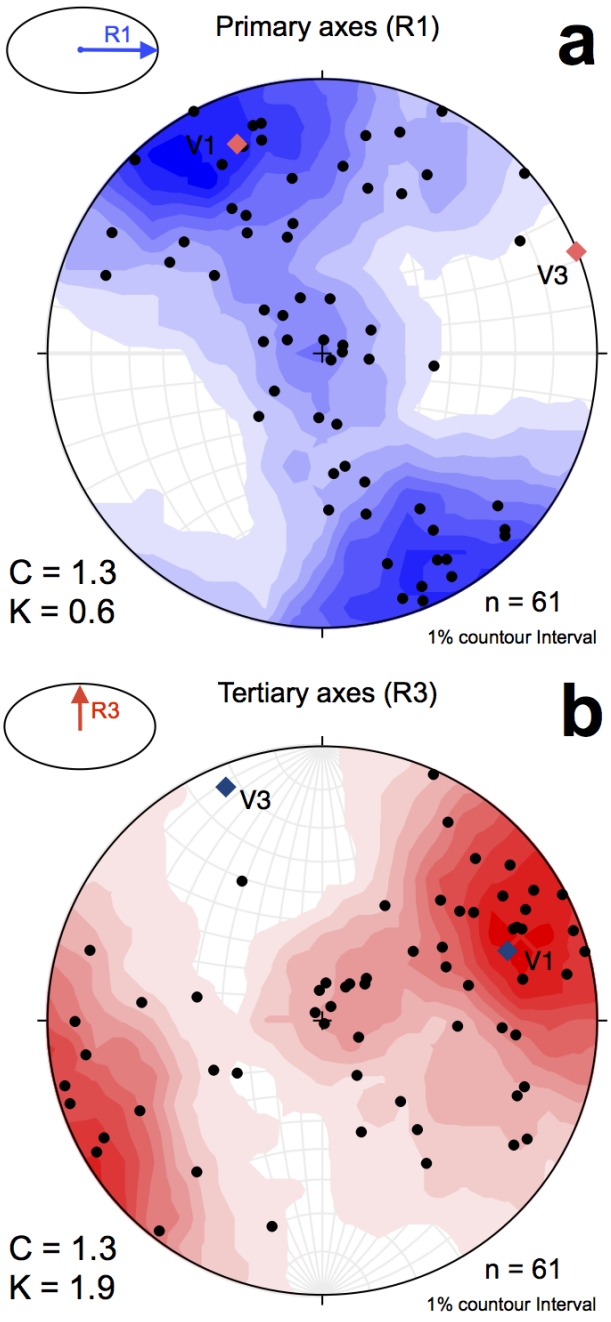

1211

1212 **Figure 9**

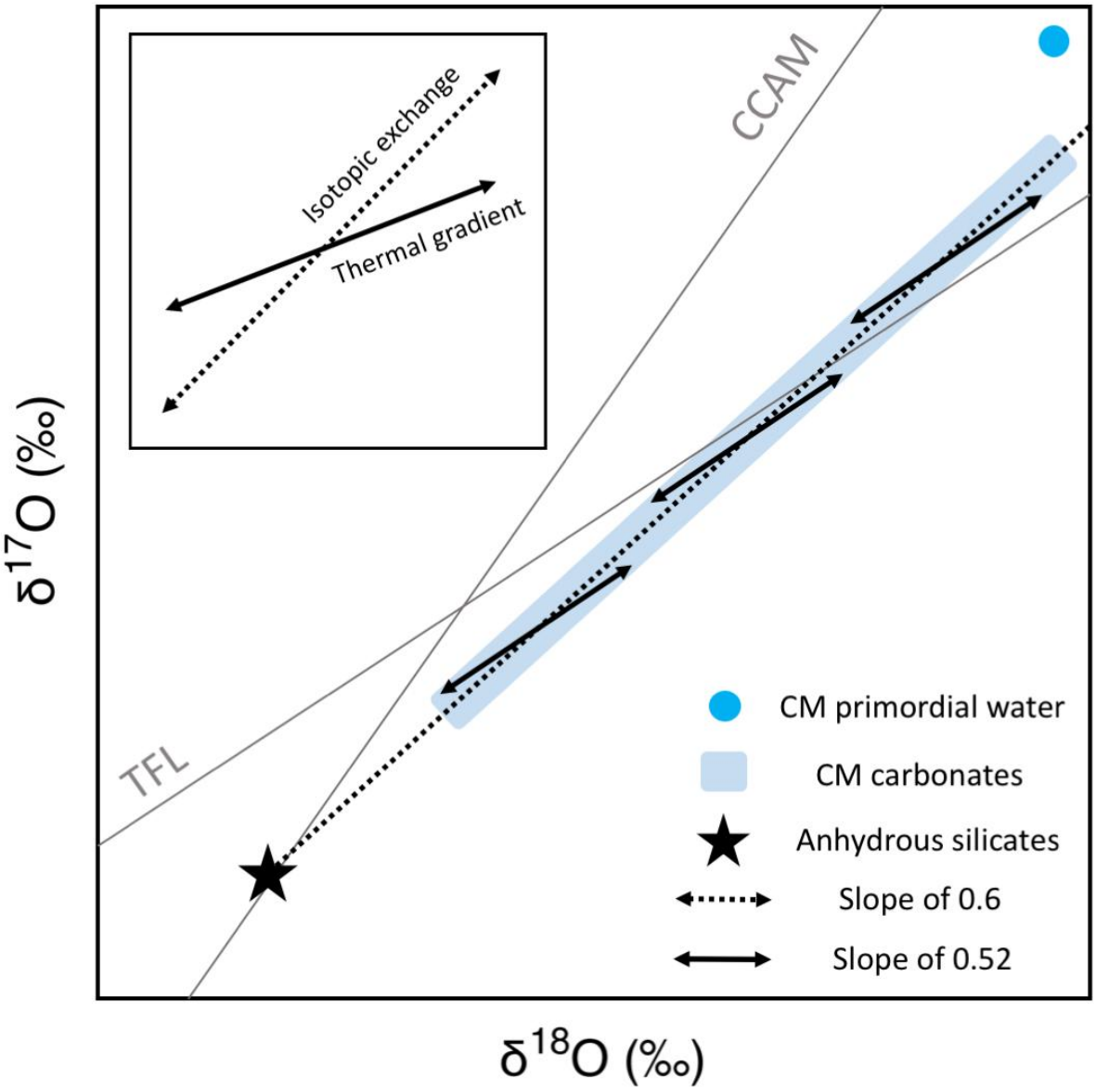

1213

1214 **Figure 10**

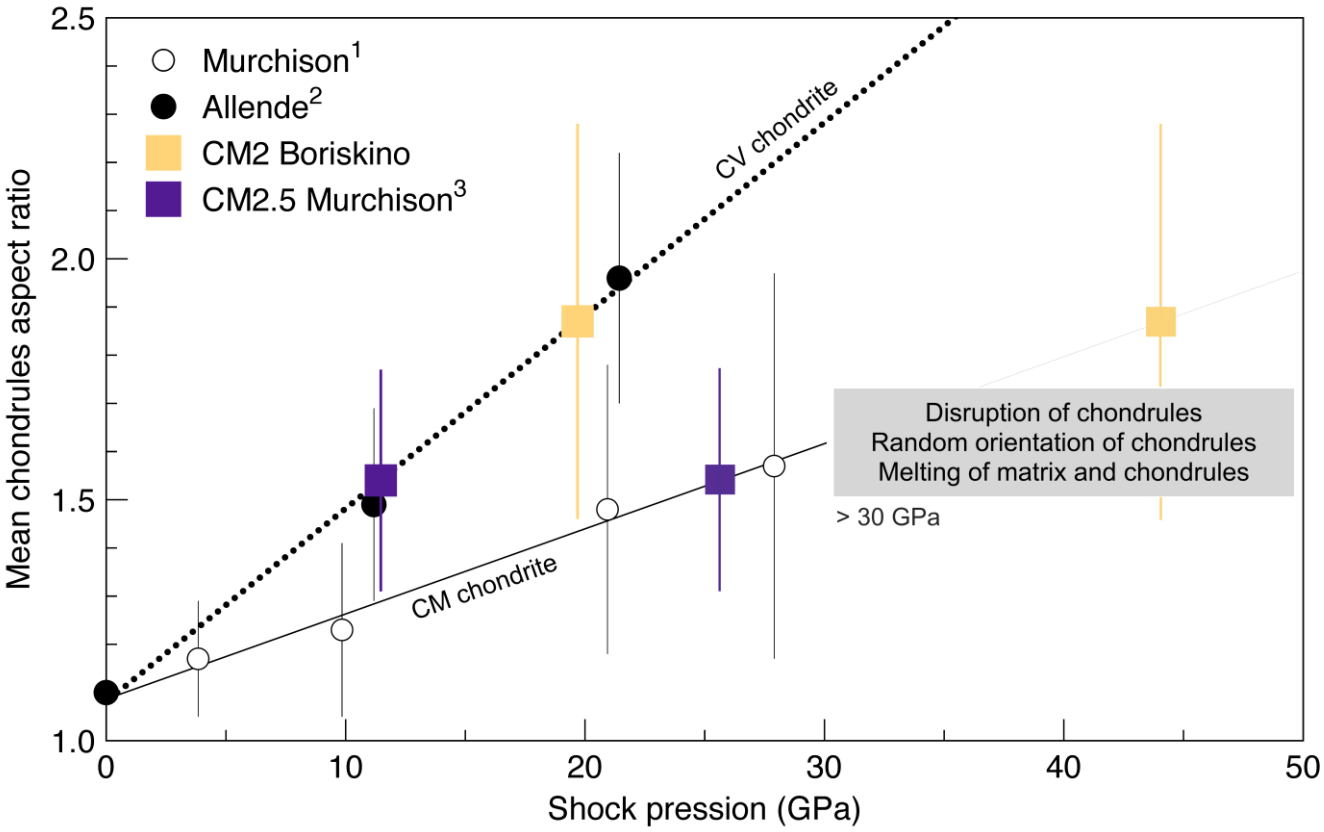
Mean chondrules aspect ratio
Shock pression (GPa)
Murchison[1]
Allende[2]
CM2 Boriskino
CM2.5 Murchison[3]
CV chondrite
CM chondrite
Disruption of chondrules
Random orientation of chondrules
Melting of matrix and chondrules
> 30 GPa
2.5
2.0
1.5
1.0
0
10
20
30
40
50

Figure 11

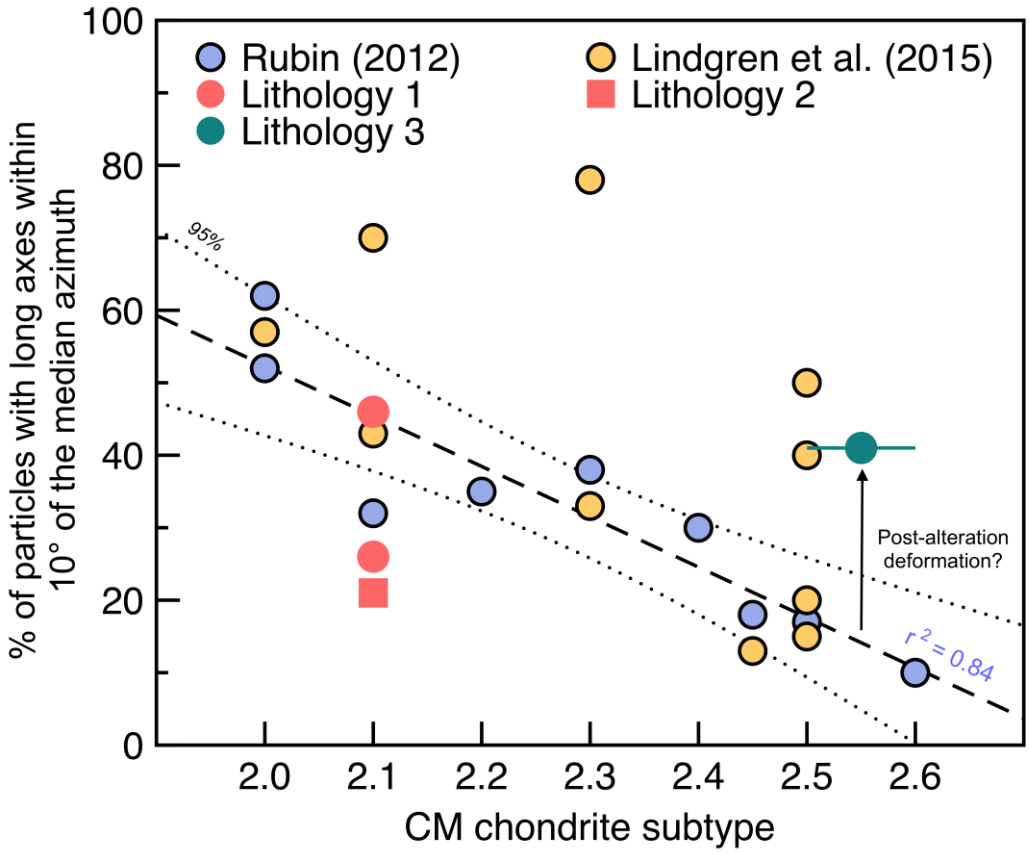

1218

1219 **Figure 12**

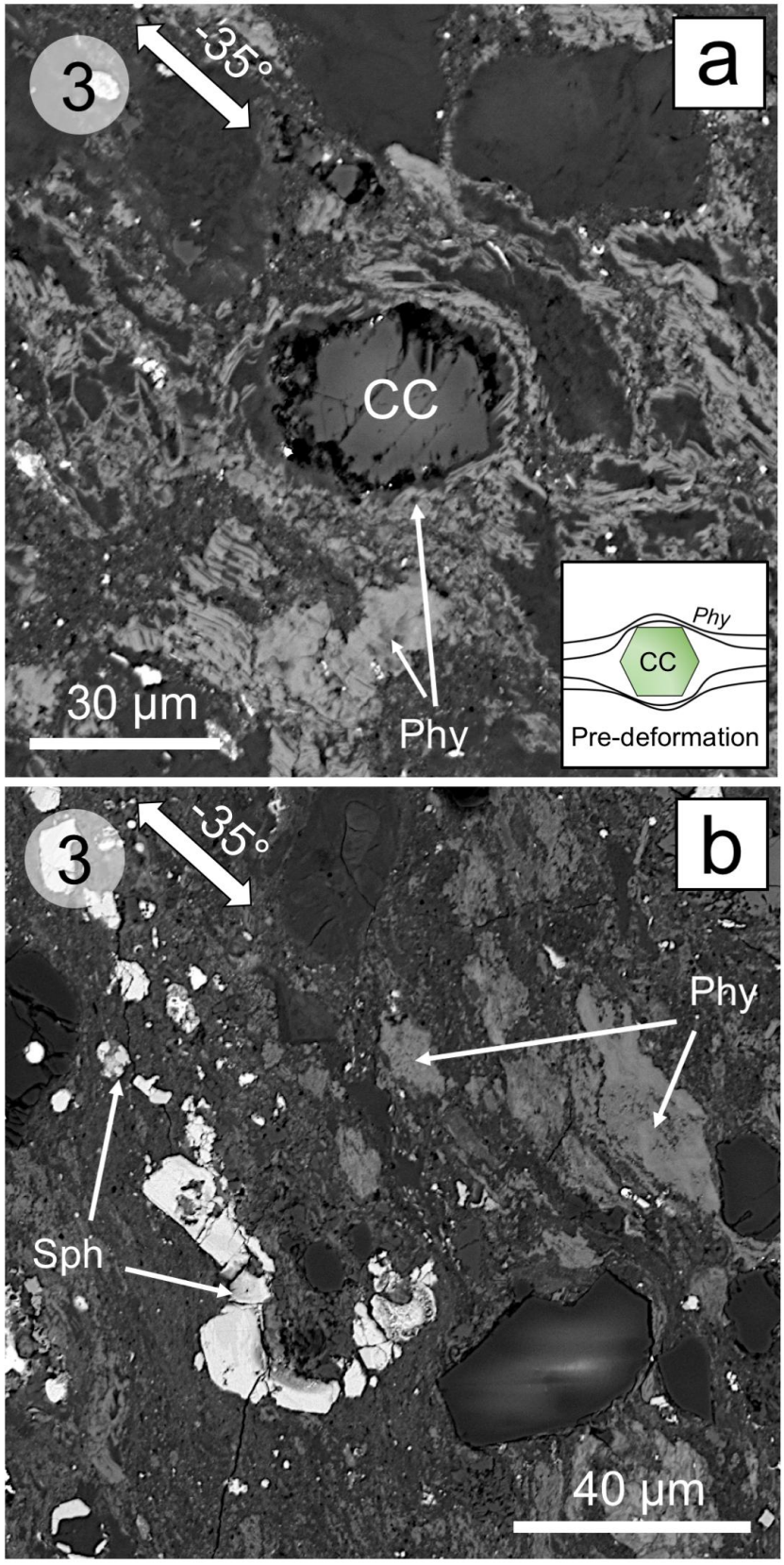

Figure 13

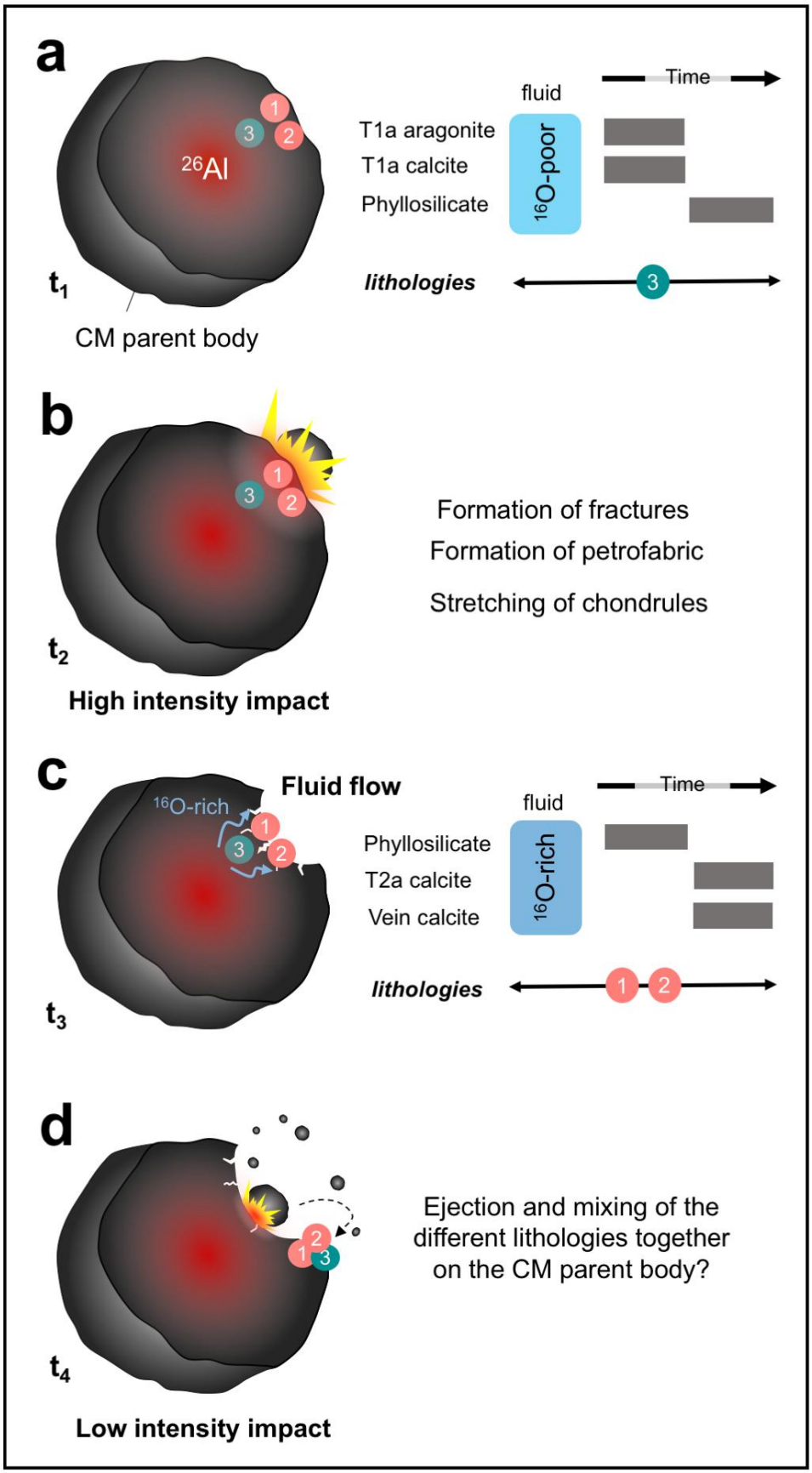

1222

1223 **Figure 14**

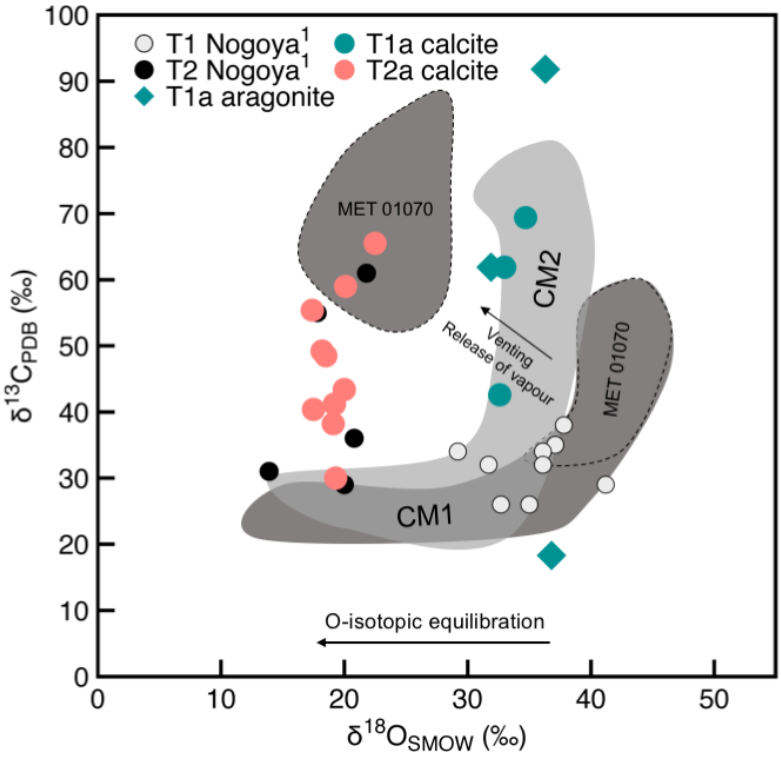

1224

1225 **Figure 15**

1226

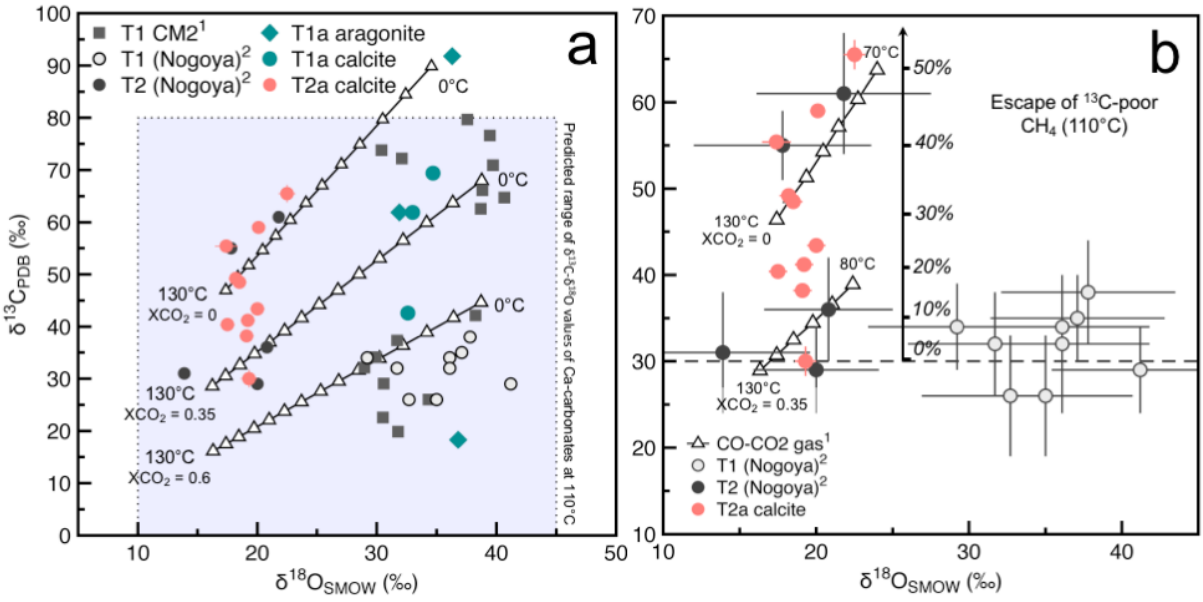
a
T1 CM2[1]
T1 (Nogoya)[2]
T2 (Nogoya)[2]
T1a aragonite
T1a calcite
T2a calcite
0°C
0°C
0°C
130°C
XCO2 = 0
130°C
XCO2 = 0.35
130°C
XCO2 = 0.6
Predicted range of δ13C-δ18O values of Ca-carbonates at 110°C
δ13CPDB (‰)
δ18OSMOW (‰)
b
Escape of 13C-poor
CH4 (110°C)
70°C
80°C
130°C
XCO2 = 0
130°C
XCO2 = 0.35
50%
40%
30%
20%
10%
0%
CO-CO2 gas[1]
T1 (Nogoya)[2]
T2 (Nogoya)[2]
T2a calcite
δ18OSMOW (‰)

Figure 16

Lithologies	L1 (n = 510)	L2 (n = 501)	L3 (n = 251)
Surface counting (mm^2)	6	4	2
Matrix (vol. %)	60.15	62.3	68
Chondrule (vol. %)	30	34.7	23.9
Sulphide (vol. %)	8.6	1.6	5.2
Ca-carbonate (vol. %)	1.2	1.4	2.4
Metallic Fe-Ni (vol. %)	~0.05	Not detected	~0.5
Chondrule mesostasis	Phyllosilicate	Phyllosilicate	Phyllosilicate
Mafic silicate into chondrule	Partially altered	Partially altered	Unaltered
Type of Ca-carbonate	T2a and veins	T2a	T1a

Table 1. Modal abundance of mixture of phases and components (in vol. %) determined by point counting and petrographic observations of section #4 of Boriskino.

	Mean	StDev	Min	Max
		(n = 61)		
Primary axis length (μm)	249	*109*	82	531
Secondary axis length (μm)	187	*79*	71	447
Tertiary axis length (μm)	132	*48*	61	300
Volume (mm^3)	0.03	*0.04*	0.002	0.2
Aspect ratio[1]	1.87	*0.46*	1.11	3.34
Elongation[2]	1.34	*0.26*	1.01	2.07
Flatness[3]	1.4	*0.29*	1.06	2.46

[1]Primary axis length/tertiary axis length
[2]Primary axis length/secondary axis length
[3]Secondary axis length/tertiary axis length

Table 2. Bulk best-fit ellipsoid measurements of dark-toned objects (interpreted as type I chondrules) in the CM Boriskino.

1284

#	Type	Polymorph	Lith.	$\delta^{18}O$ (‰)	2σ	$\delta^{17}O$ (‰)	2σ	$\Delta^{17}O$ (‰)	2σ	$\delta^{13}C$ (‰)	2σ
CC10	1a	Aragonite	(3)?	36.8	0.8	18.3	0.5	-0.8	0.8	18.3	0.6
CC4	1a	Aragonite	(3)	36.3	0.7	17.8	0.5	-1.1	0.7	91.8	0.8
CC6	1a	Aragonite	(3)	33.4	1.2	16.4	0.7	-1.0	1.1	-	-
CC5	1a	Aragonite	(3)	31.9	0.6	15.6	0.6	-0.9	0.7	61.9	1.4
CC15-1	1a	Calcite	(3)	35.4	0.7	16.6	0.6	-1.8	0.8	25.6	1.5
CC15-2	1a	Calcite	(3)	29.8	0.7	15.2	0.5	-0.4	0.7	59.6	0.5
CC3	1a	Calcite	(3)	33	0.7	16.6	0.6	-0.6	0.8	61.9	1.2
CC7-1	1a	Calcite	(3)	34.7	0.7	16.7	0.6	-1.3	0.7	71.6	0.9
CC7-2	1a	Calcite	(3)	-	-	-	-	-	-	67.2	0.9
Mean				**33.9**		**16.7**		**-1.0**		**55.8**	
StDev				*2.4*		*1*		*0.4*		*25.7*	
CC6-3	2a	Calcite	(1)	22.5	0.7	8.2	0.6	-3.5	0.8	56.8	0.9
CC6-2	2a	Calcite	(1)	-	-	-	-	-	-	68.9	0.6
CC6-1	2a	Calcite	(1)	-	-	-	-	-	-	70.7	1.3
CC11	2a	Calcite	(2)	20.1	0.5	8.8	0.6	-1.7	0.7	59	0.4
CC7	2a	Calcite	(1)	20	0.6	7.3	0.5	-3.1	0.7	43.4	0.5
CC9	2a	Calcite	(1)	19.3	0.7	7.6	0.6	-2.4	0.8	30	1.7
CC12	2a	Calcite	(2)	19.2	0.7	6.8	0.7	-3.2	0.8	-	-
CC5	2a	Calcite	(1)	19.2	0.6	7.4	0.5	-2.6	0.7	41.2	0.6
CC3	2a	Calcite	(1)	19.1	0.6	6.7	0.5	-3.3	0.7	38.2	0.6
CC10	2a	Calcite	(2)	18.6	0.7	7.2	0.6	-2.4	0.8	-	-
CC1	2a	Calcite	(1)	18.5	0.6	6.2	0.5	-3.4	0.7	48.5	0.5
CC14	2a	Calcite	(2)	18.2	0.6	7.2	0.6	-2.2	0.7	49.2	0.6
CC8-2	2a	Calcite	(1)	17.6	0.5	8.6	0.5	-0.6	0.7	-	-
CC8-1	2a	Calcite	(1)	17.2	0.8	7.1	0.7	-1.8	0.9	55.4	0.5
CC16	2a	Calcite	(3)	17.5	0.6	6.6	0.6	-2.5	0.7	40.4	0.5
Mean				**19.0**		**7.4**		**-2.5**		**50.1**	
StDev				*1.4*		*0.8*		*0.8*		*12.4*	
CC2	Vein	Calcite	(1)	16.9	0.6	6.7	0.5	-2.0	0.7	-	-

1285

1286 **Table 3**. Mineralogies, petrographic types, and oxygen and carbon isotopic compositions of
1287 Boriskino Ca-carbonates.